DISEASES AND DISORDERS

Disorganization and degeneration of liver sympathetic innervations in nonalcoholic fatty liver disease revealed by 3D imaging

Csaba Adori[1]*, Teresa Daraio[2], Raoul Kuiper[3], Swapnali Barde[1], Lubica Horvathova[4], Takashi Yoshitake[5], Robert Ihnatko[6†], Ismael Valladolid-Acebes[2], Pauline Vercruysse[2], Ashley M. Wellendorf[7], Roberto Gramignoli[3], Bela Bozoky[8], Jan Kehr[5], Elvar Theodorsson[6], Jose A. Cancelas[7,9], Boris Mravec[4,10], Carl Jorns[11], Ewa Ellis[12], Jan Mulder[1], Mathias Uhlén[1,13‡], Christina Bark[1‡], Tomas Hökfelt[1‡]

Hepatic nerves have a complex role in synchronizing liver metabolism. Here, we used three-dimensional (3D) immunoimaging to explore the integrity of the hepatic nervous system in experimental and human nonalcoholic fatty liver disease (NAFLD). We demonstrate parallel signs of mild degeneration and axonal sprouting of sympathetic innervations in early stages of experimental NAFLD and a collapse of sympathetic arborization in steatohepatitis. Human fatty livers display a similar pattern of sympathetic nerve degeneration, correlating with the severity of NAFLD pathology. We show that chronic sympathetic hyperexcitation is a key factor in the axonal degeneration, here genetically phenocopied in mice deficient of the Rac-1 activator Vav3. In experimental steatohepatitis, 3D imaging reveals a severe portal vein contraction, spatially correlated with the extension of the remaining nerves around the portal vein, enlightening a potential intrahepatic neuronal mechanism of portal hypertension. These fundamental alterations in liver innervation and vasculature uncover previously unidentified neuronal components in NAFLD pathomechanisms.

INTRODUCTION

Nonalcoholic fatty liver disease (NAFLD) is the most common liver disorder, with a prevalence of around 25% in Western countries (1, 2). NAFLD, often considered as the hepatic manifestation of metabolic syndrome, is usually associated with visceral obesity, insulin resistance, increased blood pressure, fasting hyperglycemia, type 2 diabetes, and dyslipidemia (2, 3). The spectrum of NAFLD is broad, from simple steatosis (intrahepatic triglyceride accumulation), via nonalcoholic steatohepatitis (NASH; up to 30% of all NAFLD cases) (3, 4), to liver cirrhosis and hepatocellular carcinoma (5). While simple steatosis is a relatively benign condition, NASH is a severe disease, characterized by heavy steatosis, lobular inflammation, hepatocellular injury, and progressive fibrosis (5). Moreover, therapies aimed at NASH to reduce the risk of hepatocellular carcinoma are sparse and largely unsuccessful (6). The pathogenesis of NAFLD is complex. Initial metabolic disturbances, such as insulin resistance, may lead to steatosis, while the transition between steatosis and NASH could be described by a "multiple-hit" model: Impaired lipid partitioning, oxidative stress caused by lipotoxicity, proinflammatory cytokine-mediated hepatocyte injury, and further metabolic abnormalities may contribute to the development of NASH (7).

Recent studies emphasize the pivotal role of a vegetative imbalance, such as an increased sympathetic and a decreased parasympathetic nerve tone, in the etiopathogenesis and progression of NAFLD (8–10). Increased sympathetic outflow was described in patients with NAFLD (11, 12). In Vav3 knockout mice with chronic sympathetic hyperexcitation, the metabolic syndrome and fatty liver were noted already at 4 months of age, which developed to steatohepatitis without obesity after 1 year in animals kept on normal chow diet (13). A recent study depicted a more direct pathogenic link between liver sympathetic outflow and hepatic steatosis (14). Namely, diet-induced NAFLD in mice was associated with a doubling of firing rate of the liver sympathetic nerves, and the steatosis was effectively reversed with chemical sympathectomy, independently of changes in body weight, caloric intake, or adiposity. Overall, these findings suggest that sympathetic overactivity is a key driver of hepatic steatosis, and they highlight the role of liver nerves in the pathogenesis of NAFLD.

The hepatic innervation has, for a long time, been less in focus, mainly because liver functions did not appear seriously compromised after orthotropic liver transplantation (OLT) (15). However, long-term follow-up studies described dyslipidemia, postprandial hyperglycemia, insulin resistance, and alterations in intrahepatic microcirculation after OLT (16, 17). Neurobiological studies on liver have revealed a complex role of hepatic innervation in the regulation of liver lipid

[1]Department of Neuroscience, Karolinska Institutet, 17177 Stockholm, Sweden. [2]The Rolf Luft Research Center for Diabetes and Endocrinology, Department of Molecular Medicine and Surgery, Karolinska Institutet, 17176 Stockholm, Sweden. [3]Department of Laboratory Medicine, Karolinska Institutet, 17177 Stockholm, Sweden. [4]Biomedical Research Center, Institute of Experimental Endocrinology, Slovak Academy of Sciences, Bratislava, Slovak Republic. [5]Department of Physiology and Pharmacology, Karolinska Institutet, 17177 Stockholm, Sweden. [6]Department of Clinical Chemistry and Department of Clinical and Experimental Medicine, Linköping University, 58285 Linköping, Sweden. [7]Division of Experimental Hematology and Cancer Biology, Cincinnati Children's Hospital Medical Center, Cincinnati, OH 45229-3039, USA. [8]Department of Clinical Pathology/Cytology, Karolinska University Hospital, Huddinge, Sweden. [9]Hoxworth Blood Center, University of Cincinnati College of Medicine, Cincinnati, OH 45267-0055, USA. [10]Institute of Physiology, Faculty of Medicine, Comenius University in Bratislava, Slovak Republic. [11]PO Transplantation, Karolinska University Hospital Huddinge, 141 52 Stockholm, Sweden. [12]Department of Transplantation Surgery and Department of Clinical Science, Intervention and Technology (CLINTEC), Karolinska University Hospital, Karolinska Institutet, 17177 Stockholm, Sweden. [13]Science for Life Laboratory, Royal Institute of Technology, 10691 Stockholm, Sweden.
*Corresponding author. Email: adorics@gmail.com
†Present address: Institute of Pathology, University Medical Center, Georg-August University of Göttingen, Göttingen, Germany.
‡These authors contributed equally to this work.

and glucose metabolism, hemodynamics, immune processes, bile secretion, and regeneration (17–20).

Studies of liver nerves in pathological conditions are sparse, and even those few ones in human mainly focus on hepatitis or cirrhosis and mostly apply less specific nerve markers, such as S100 (21–25). However, a comprehensive examination of the liver innervation in early stages of NAFLD is lacking, in both human and experimental animal models. One key obstacle in exploring hepatic nerves is the limited sectional view provided by the traditional two-dimensional (2D) imaging techniques. However, state-of-the-art volume imaging offers large-scale 3D visualization with cellular resolution, allowing detailed examination of the full nerve arborizations in tissue blocks.

Application of volume imaging technologies is, today, in the front-line of system biological studies (26). The innervations of adipose tissue, pancreas, and lung have recently been explored using iDISCO (immuno-enabled three-dimensional imaging of solvent cleared organs) volume imaging technique (27–29). Literature concerning liver tissue optical clearing is, however, up until now, limited; successful clearing on rodent liver with CLARITY (30) or other techniques, including CUBIC (clear, unobstructed brain/body imaging coctails and computational analysis), 3DISCO, or SeeDB (See Deep Brain clearing) (31), was reported in methods papers.

In the present study, we applied iDISCO+ volume immuno-imaging and various biochemical methods to explore the integrity of the liver innervation at different stages of experimental NAFLD. Since long nonmyelinated monoaminergic nerve fibers are particularly vulnerable to oxidative stress and other toxic effects (32–34), we hypothesized that chronic hepatic nervous overactivity and oxidative challenges in NAFLD may be associated with pathological alterations of the liver sympathetic nerves. Indeed, we observed a disorganization of the sympathetic innervation in wild-type (WT) steatotic mice fed on Western diet (WD) for 7 weeks and a severe degeneration of the same arborization in heavy steatohepatitis in *SNAP-25b*–deficient mice kept on WD. Human fatty livers showed a similar sympathetic nerve degeneration profile, which is correlated with the severity of NAFLD pathology.

RESULTS
Study design to explore mouse liver innervation in 3D
We applied the iDISCO+ volume immunostaining and clearing technology combined with light sheet fluorescence microscopy to explore the detailed 3D organization of the mouse liver innervation and vascular structures. Tyrosine hydroxylase (TH) 3D staining of the entire left lateral liver lobe revealed that noradrenergic (NAergic) nerve axons/terminals form a repetitive network innervating the four major portal branches of the lobe (Fig. 1A). In the subsequent experiments, the left lateral lobe was cut into four equal pieces (ca. 5 mm by 5 mm by 4 mm), each of them containing one main portal branch (Fig. 1B). This sample shape/size was optimized to obtain efficient antibody penetration and clearing quality, reasonable scanning time and file size, with a resolution that allowed study of the 3D structure and pathology, even of individual nerve fibers. The four pieces were volume-immunostained for (i) TH, thus a marker for NAergic/sympathetic nerves; (ii) PGP9.5 (protein gene product 9.5), a pan-neuronal marker; (iii) the vesicular acetylcholine transporter (VAChT), a marker for cholinergic, parasympathetic nerves; and (iv) calcitonin gene-related peptide (CGRP), a marker for primary sensory nerves, according to the scheme reported in Fig. 1B.

Sympathetic (NAergic) innervation of the mouse liver in 3D
3D segmentation of the portal area and central veins based on inverted tissue 488 autofluorescence (AF) (fig. S1A) confirmed the dense periportal NAergic innervation (Fig. 1, C and D). More detailed manual segmentation of the components of a 3-mm-long main portal branch [based on AF, α–smooth muscle actin (αSMA) + cytokeratin 7 (CK7), and αSMA + TH 3D stainings; fig. S1, B to E, and movie S1] revealed that "major" thick nerve fibers (diameter, 8 to 20 μm) ran primarily around the hepatic artery and bile duct. In addition, "thinner" tracts (diameter, 3 to 4 μm) originating from the discrete thick fibers formed a dense network around all elements of the portal triad (Fig. 1, E and F, and movie S2). These fine vari-cose nerve filaments terminated just 100 to 200 μm ahead of the end of the most distal portal veins, 300 to 400 μm below the organ surface (Fig. 1, G to J).

The NAergic innervation of portal tracts was confirmed using 2D sections stained for TH and neuropeptide Y (NPY) or galanin, two neuropeptides that colocalize in NAergic neurons (35) (Fig. 1H and fig. S1, J to K). High-resolution confocal analyses showed that the complex, fine sympathetic portal innervations followed extra-cellular matrix (ECM) fibers in the Glisson's capsule (TH + collagen III costaining) and provided close contacts with vascular smooth muscle cells and endothelial cells in the hepatic artery and portal vein wall, as well as with biliary epithelial cells of the bile ducts, using appropriate markers (Fig. 1I and fig. S1, F to H). Central veins were typically not innervated by NAergic nerves, except for sparse TH-positive (TH+) fibers around thicker central branches (Fig. 2, A and B). Such fibers originated from individual NAergic nerves emerging from adjacent portal tracts. These single "bridging" fibers branched again around the central vein wall and extended for a few hundred micrometers (Fig. 2, A and B, arrows).

WT mice and *SNAP-25b*–deficient mice on WD are models for steatosis and steatohepatitis, respectively
The sympathetic nerves in fatty liver were studied in the *SNAP-25b*–deficient mouse line [mutant (MT)] and WT littermates kept on high-fat/high-sucrose diet (Western diet, WD) for 7 weeks (MT + WD and WT + WD, respectively). The WD groups were compared to WT animals fed on a standard chow diet used as controls (CoD). The metabolic status of these mice has been extensively character-ized earlier. Namely, WT + WD mice exhibited increased body weight/body mass index, elevated preprandial blood cholesterol and triglyceride levels, increased basal serum leptin and hepatic tri-glyceride levels, and impaired glucose homeostasis, all compared to CoD. All these symptoms were also present in MT + WD mice but were more aggravated. Moreover, calculation of insulin resistance index [(HOMA$_{IR}$; homeostatic model assessment of insulin resistance)] revealed a tendency of increase in WT + WD and a strongly signif-icant increase in MT + WD. Together, both WD groups exhibit obesity and features of the metabolic syndrome, while the MT group in addition shows clear signs of diabesity (36).

In agreement with earlier findings, WT + WD and MT + WD mice showed increased body weight (Fig. 3B). Hematoxylin-eosin and quantified Oil Red O (ORO) lipid staining indicated steatosis in the WT + WD group, as well as severe steatosis and indications for he-patocellular ballooning in the MT + WD animals (Fig. 3, A and C). The immunostaining densities for the macrophage markers F4/80 and Iba-1 increased in both groups, compared to control, reaching the level of statistical significance already in WT + WD in the case
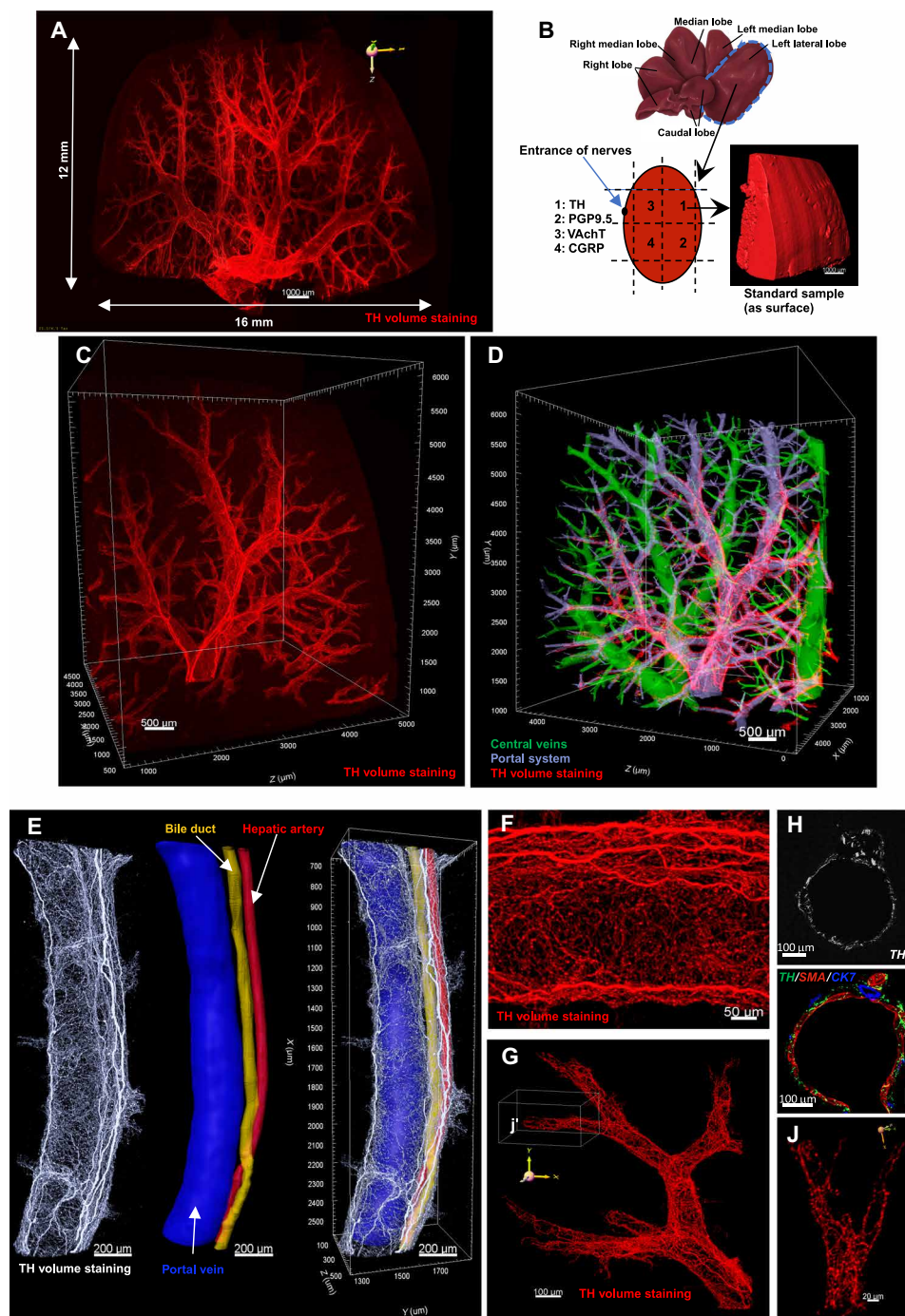
Fig. 1. Sampling principles and sympathetic innervation of the mouse liver. (**A**) TH 3D staining of the full left lateral lobe of a control mouse. (**B**) Principle of sampling strategy. (**C**) TH 3D staining of a standard control sample block. (**D**) TH 3D staining + segmented surfaces covering the portal area and the central veins. (**E**) TH 3D staining + segmentation of the portal triad. (**F**) TH 3D staining: zoom to a major portal branch. (**G**) TH labeling: zoom to a terminal portal branch. The boxed zone (j') is enlarged in (**J**). (**H**) TH 2D staining: portal triad innervation. (**I**) TH + αSMA + CK7 triple labeling of a portal triad. Scale bar is indicated in each micrograph.

of F4/80 but only in MT + WD in the case of Iba-1 (Fig. 3, A, D, and E). The number of liver inflammatory foci slightly increased in the WT + WD group and strongly increased in MT + WD (Fig. 3, F to H). Only in the MT + WD group did Picro Sirius Red show increased amount of collagen fibers, indicating fibrosis (Figure 3I), while 3D staining for CK7 depicted epithelial cell proliferation, indicating a ductal reaction (Fig. 3, J and K). Overall, all these results suggest a moderate liver steatosis with starting inflammation in the WT + WD group and a severe steatosis with inflammation and fibrosis (steatohepatitis) in the MT + WD mice.
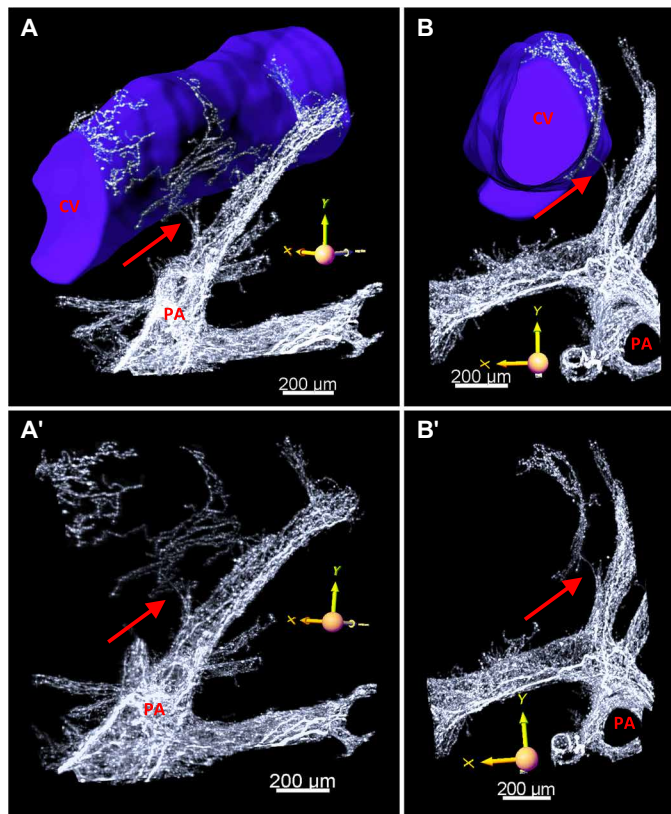
Fig. 2. The limited sympathetic central vein innervation of the mouse liver. (**A** and **B**) A bridging NAergic fiber (arrow), originating from the dense periportal innervation, branches again in the central vein wall providing a limited central vein innervation. (A) and (B) show the same adjacent portal and central branches from different 3D perspectives. (**A′** and **B′**) The same portal and central nerve branches like in (A) and (B), respectively, without the segmented central vein. TH volume immunostaining (gray). PA, portal area; CV, central vein (segmented based on tissue AF). Scale bars are indicated in each panel.

Axonal pathology, disorganization, and gradual degeneration of sympathetic fibers in steatosis/steatohepatitis mouse models

TH 3D staining in the WT + WD group revealed disorganization, frequently swollen axonal varicosities, and mild retraction of fine, distal NAergic branches (Figs. 4, B and E versus A and D, 5, F versus D, and 6B). Moreover, individual fine NAergic fibers often left the Glisson's capsule and entered the liver parenchyma (Fig. 5, B versus A, C, and E). In the MT + WD group, abundant swollen axonal varicosities were observed along the entire innervation. The fine distal fibers were severely trimmed, and the distal branches had completely disappeared. The remaining fibers were disorganized, curly, and frequently showing a discontinuous staining, both in the main (thick) and fine fiber networks (Fig. 4, C, F, G, and H versus A and D, and movie S3). Fine fibers entering the parenchyma were rarely noticed. Moreover, the total sample TH$^+$ fiber volume (Fig. 4, I to K), noradrenaline (NA) levels measured by high-performance liquid chromatography (HPLC) (Fig. 4L), and galanin levels measured by radioimmunoassay (Fig. 4M) were all significantly decreased in the MT + WD group, but not in the WT + WD group, compared to control. The

severe swollen axonal pathology and fiber degeneration were confirmed also by PGP9.5 3D staining in MT + WD samples (Fig. 4, N to P).

Next, we worked out a 3D quantification strategy to characterize the distal fine fiber retraction and the main thick-fiber alterations (for technical details, see the Supplementary Materials). Combination of inverted 488 AF and TH 3D staining allowed simultaneous visualization of the NAergic fiber arborization and the liver vasculature. The average distance of TH$^+$ fine fiber endings and the corresponding portal vein endings tended to increase in the WT + WD group and were significantly longer in the MT + WD group. However, the average distance between portal vein endings and liver surface did not change in either group (Fig. 6, A to E). The major (thick) fiber arborization was traced using the Imaris Filament tracer with 8-μm seeding points (Fig. 6F). No significant alterations were noted in the WT + WD group. In the MT + WD, however, full branch depths and level, total filament length, the number of branching points, the number of segments, the mean branching angle, and the convex hull volume of the filament structure were all significantly decreased, indicating a shorter, less complex, and less extended fiber structure in the traced 8- to 20-μm filaments (Fig. 6, G to J, and fig. S3A). Plotting the branching angles revealed that, in particular, branches with higher branching angles decreased in number, indicating a preferential loss of distal fiber branches (fig. S3, B to E).

SNAP-25b–deficient mice on control diet do not show NAergic fiber degeneration

To explore the possibility that the *SNAP-25b* deficiency itself may cause sympathetic nerve degeneration in the liver, we examined MT animals kept on CoD (versus WT animals on CoD) (Fig. 7, A to I, and figs. S2 and S3). Moreover, all quantified parameters of sympathetic fibers as well as hepatic NA levels were demonstrated and statistically evaluated together with the WT + CoD, WT + WD, and MT + WD groups (fig. S2 and tables S5 and S6). The MT + CoD group did not show alterations compared to WT + CoD in any of the examined filament tracing parameters (Fig. 7I and figs. S2, E to L, and S3, B to E) or in the total sample TH+ fiber volume (Fig. 7E and fig. S2A), in TH$^+$ fiber end versus corresponding portal vein end distances (Fig. 7, F and G, and fig. S2, C and D), or in the NA levels measured by HPLC (Fig. 7H and fig. S2B). Thus, *SNAP-25b* deficiency per se does not lead to NAergic fiber degeneration. The severe sympathetic nerve pathology noticed in the MT + WD animals was rather related to the serious metabolic impairments and steatohepatitis caused by a combination of WD and the mutation.

The disorganization of NAergic fibers is paralleled by perturbation of the periportal collagen III fiber network and increased NGF expression in steatosis

Collagen fibers start to reorganize early in hepatic steatosis (*37*, *38*). Confocal microscopy analysis showed that thick collagen III$^+$ fibers frequently left the portal area and penetrated the parenchyma in the WT + WD group. TH$^+$, NAergic nerve fibers that left the Glisson capsule and entered the parenchyma always followed these collagen fibers (Fig. 8, A to C).

Since nerve growth factor (NGF) is a highly expressed neurotrophic factor in the mouse liver, and ectopic NGF expression is sufficient for modulating the intrahepatic nerve network in mouse (*39*), we examined hepatic NGF gene expressions in our samples. NGF was significantly upregulated in the WT + WD (steatosis) group (Fig. 8D), where we observed frequent sympathetic fiber
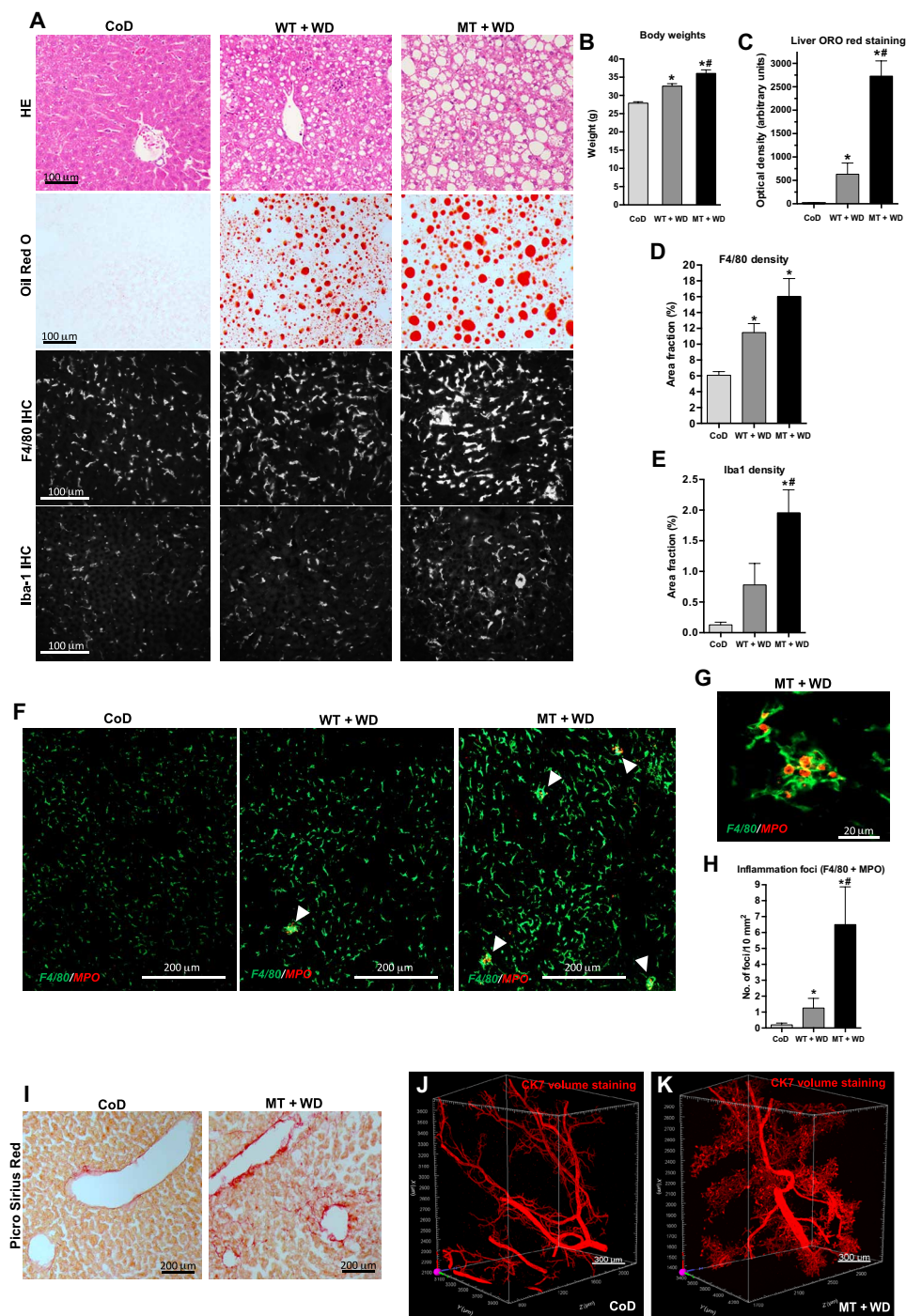
Fig. 3. Liver pathology of *SNAP-25b*–deficient mice and WT littermates on 7-week WD (MT + WD and WT + WD, respectively). (**A**) Representative micrographs of livers from control (CoD: WT, normal chow diet), WT + WD, and MT + WD stained for hematoxylin-eosin (HE), ORO lipid histochemistry, and F4/80 and Iba-1immunomarkers. (**B**) Body weight measurements, *n* = 15 to 18 per group. (**C** to **E**) Quantifications of ORO (C) and F4/80 (D) and Iba-1 (E) staining, *n* = 5 to 7 per group. (**F**) F4/80 and myeloperoxidase (MPO) double staining. Arrowheads: inflammatory foci. (**G**) High magnification of an inflammatory focus. (**H**) Quantification of inflammatory foci, *n* = 5 to 7 per group. (**I**) Picro Sirius Red collagen histochemistry on MT + WD versus CoD livers. (**J** and **K**) CK7 3D staining of CoD (J) and MT + WD (K) samples. *$P < 0.05$, CoD versus MT + WD; #$P < 0.05$, WT + WD versus MT + WD. Data expressed as means ± SEM. Scale bar is indicated in each micrograph.

sprouting to the parenchyma. However, there was no increase in NGF expression in the MT + WD (steatohepatitis) group but rather a tendency toward a decrease (Fig. 8D), despite the intense proliferation of collagen fibers, suggesting fibrosis in this group (Fig. 3I). Neurotrophin-5, another albeit much lower expressed neurotrophic factor in the murine liver (*39*), was not up-regulated in the WT + WD group but was significantly down-regulated in the MT + WD group (Fig. 8E).
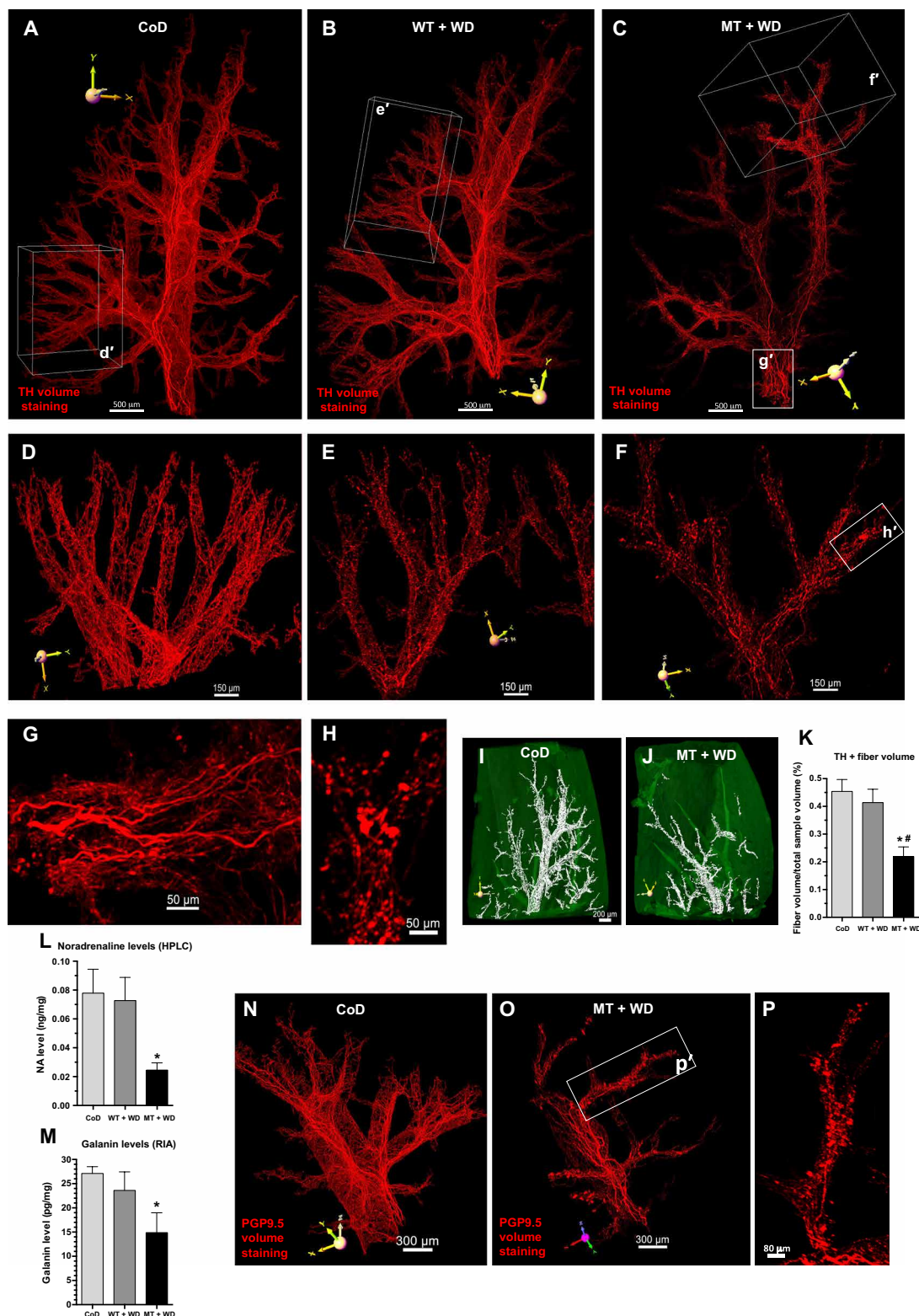
Fig. 4. NAergic nerve fiber pathology in experimental steatosis (WT + WD) and steatohepatitis (MT + WD) in 3D. (**A** to **F**) TH 3D staining of CoD (A and D), WT + WD (B and E), and MT + WD (C and F) samples. Boxed volumes in (A), (B), and (C) [(d′), (e′), and (f′), respectively] are enlarged in (D), (E), and (F), respectively. (**G** and **H**) Zoom of proximal (G) and distal (H) TH⁺ fiber branches in MT + WD. Boxed zones in (C) and (F) [(g′) and (h′), respectively] are enlarged in (G) and (H), respectively. (**I** to **K**) Quantification (K) of total TH⁺ fiber volume in CoD (I) and in MT + WD (J). (**L** and **M**) Measurement of liver NA (L) and galanin (M) levels. (**N** to **P**) PGP9.5 3D staining in CoD (N) and in MT + WD (O). Boxed zone in (O) [(p′)] is enlarged in (P). *$P < 0.05$, CoD versus MT + WD; #$P < 0.05$, WT + WD versus MT + WD. Data expressed as means ± SEM, $n = 5$ to 7 per group. Scale bar is indicated in each micrograph.
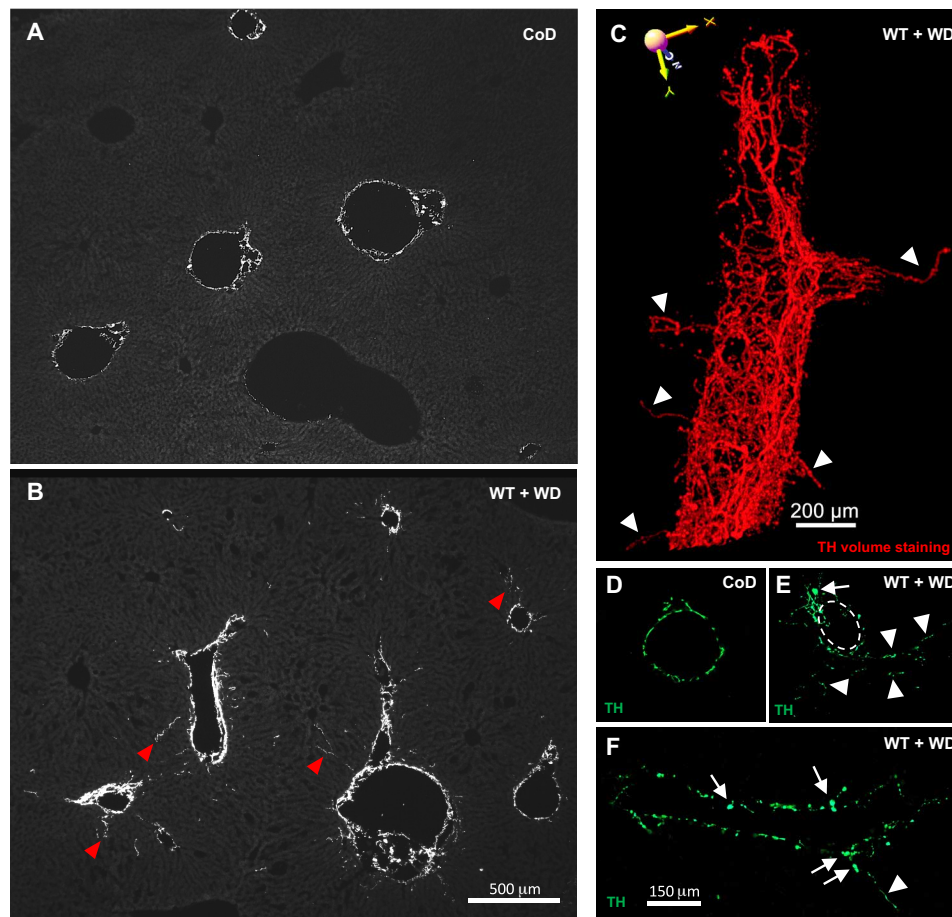
Fig. 5. Sympathetic nerve sprouting to the parenchyma in the WT + WD (steatosis) group. (**A** and **B**) TH immunostaining of control (A) and WT + WD (B) mouse liver. Note that NAergic fibers leave the portal area and enter the parenchyma in WT + WD (arrowheads). (**C**) TH volume immunostaining of WT + WD. Arrowheads: NAergic fine fibers entering the parenchyma. (**D** to **F**) Confocal imaging of the NAergic innervation of portal branches from control (D) and WT + WD livers (E and F). Arrows: swollen varicosities; arrowheads: fibers growing to the parenchyma. Dashed line in (E): contour of the portal vein. Scale bar in (B) applies to (A) and (B). Scale bar in (F) applies to (D) to (F).

Vav3^{−/−} mice with chronic sympatho-excitation exhibit swollen NAergic axonal pathology

Chronic sympathetic overexcitation has been described in obesity and the metabolic syndrome (*11*, *12*). In this context, we examined the integrity of NAergic innervations in the liver of *Vav3*^{−/−} mice that show chronic sympathetic hyperexcitation due to the lack of Vav3, a Rac-1 activator. Notably, these mice develop the metabolic syndrome and steatosis at the age of 4 months and steatohepatitis by 12 months of age, without any obesity (*13*). TH 3D staining in the liver of 4-month-old *Vav3*^{−/−} mice revealed frequent swollen axonal varicosities and reduction in the fine axonal network in distal-end branches, similarly to WT + WD animals (Fig. 8, F to I). Moderate hepatic steatosis without fibrosis was noticed in the liver of Vav3^{−/−} mice (Fig. 8, J to M).

Decreased gene expression of α-/β-adrenergic receptors and connexin32 gap junction protein in steatosis and steatohepatitis

As the next step, we explored expression of some key molecules that are involved in the signal transmission of the released NA. *Aα1b*

and *Aβ3* gene expression decreased significantly in the WT + WD group, and the expressions of four examined adrenoreceptors (*Aα1b*, *Aα1d*, *Aβ2*, and *Aβ3*) were down-regulated in MT + WD (Fig. 8, W to Z).

In addition, we studied expression of connexin 32 (*Cx32*), the main component of mouse liver gap junctions (*40*). Since the innervation is restricted to the portal area in mouse and rat liver, the highly abundant gap junctions on hepatocytes (Fig. 8N) have a critical role in transducing the NAergic signal (*41*). *Cx32* mRNA expression was significantly decreased in both WT + WD and MT + WD groups, compared to control (Fig. 8O). Moreover, CX32 immunostaining showed decreased protein expression throughout the liver in both WT + WD and MT + WD samples (Fig. 8, P to V).

3D reconstruction reveals portal vein stenotic alteration in a mouse model of steatohepatitis

Since adrenergic receptors in the portal vein wall mediate vasomotor effects (*42*), we next studied the morphology of the portal area and also the central veins in 3D, using the inverted AF method (fig. S1A). In the MT + WD group, the portal area had seemingly shrunk (Fig. 9, A to D). Total portal area volume was significantly decreased, while
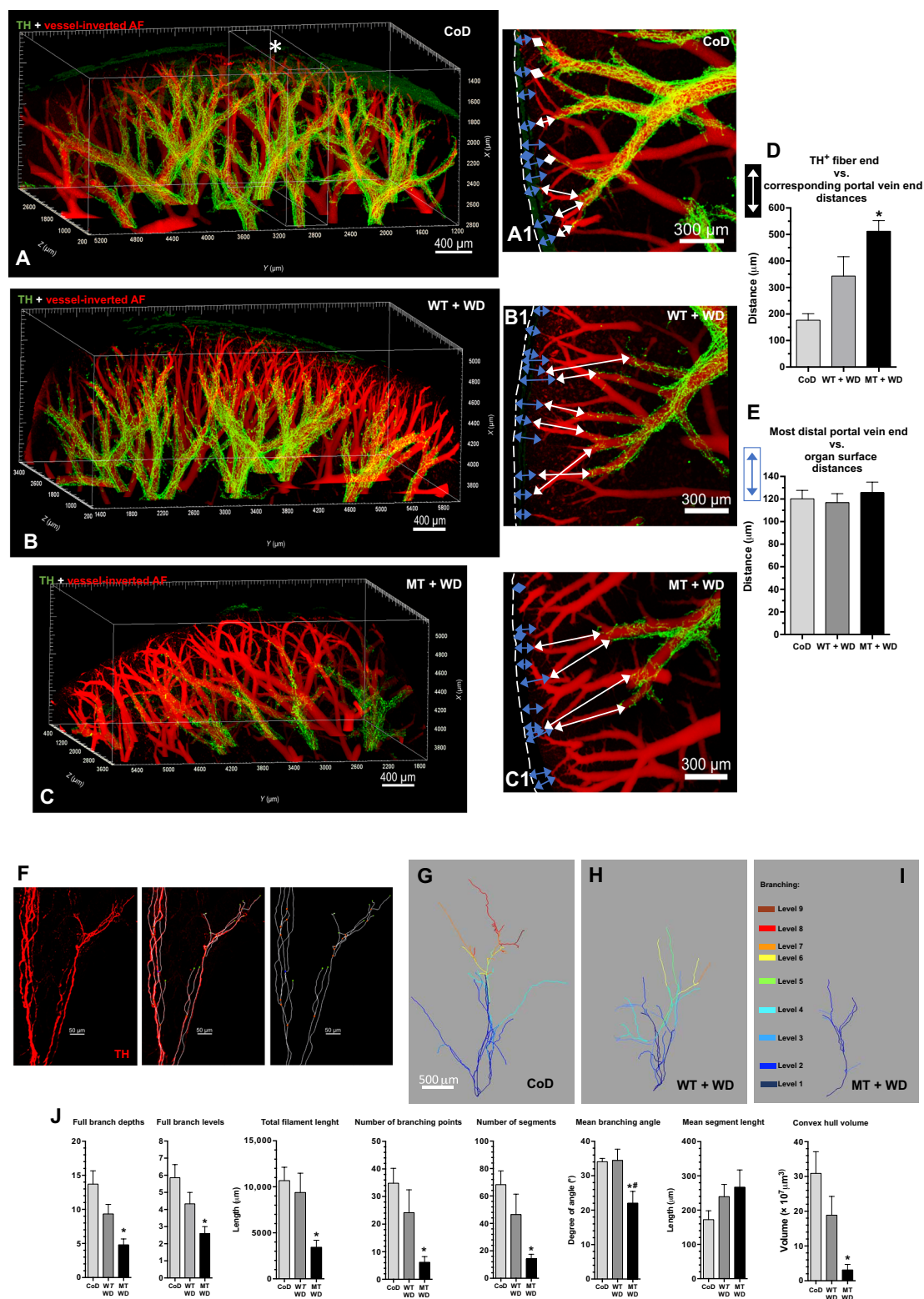
Fig. 6. Quantification of NAergic nerve fiber degeneration in mouse liver. (**A** to **C**) Gradual retraction of distal TH$^+$ nerve endings in WT + WD (B) and in MT + WD (C) versus CoD (A). (**A1** to **C1**) 2D projected pictures from 500-μm-thick virtual rectangles [an example in (A) is indicated with *]. (**D** and **E**) Quantification of TH$^+$ fiber ending/ corresponding portal vein ending distances [(D); white arrows in (A1) to (C1)] and most distal portal vein ending/organ surface distances [(E); blue arrows in (A1) to (C1)]; $n = 5$ to 6 per group. (**F**) Tracing main fiber bundles (diameter > 8 μm). (**G** to **I**) Representative examples for traced main NAergic fiber arborizations in entire samples in CoD (G), WT + WD (H), and MT + WD (I). Branching levels are color-coded as indicated in (I). (**J**) Quantification of main fiber structures; $n = 5$ to 7 per group. *$P < 0.05$, CoD versus MT + WD; #$P < 0.05$, WT + WD versus MT + WD. Data expressed as mean ± SEM. Scale bar is indicated in each micrograph.
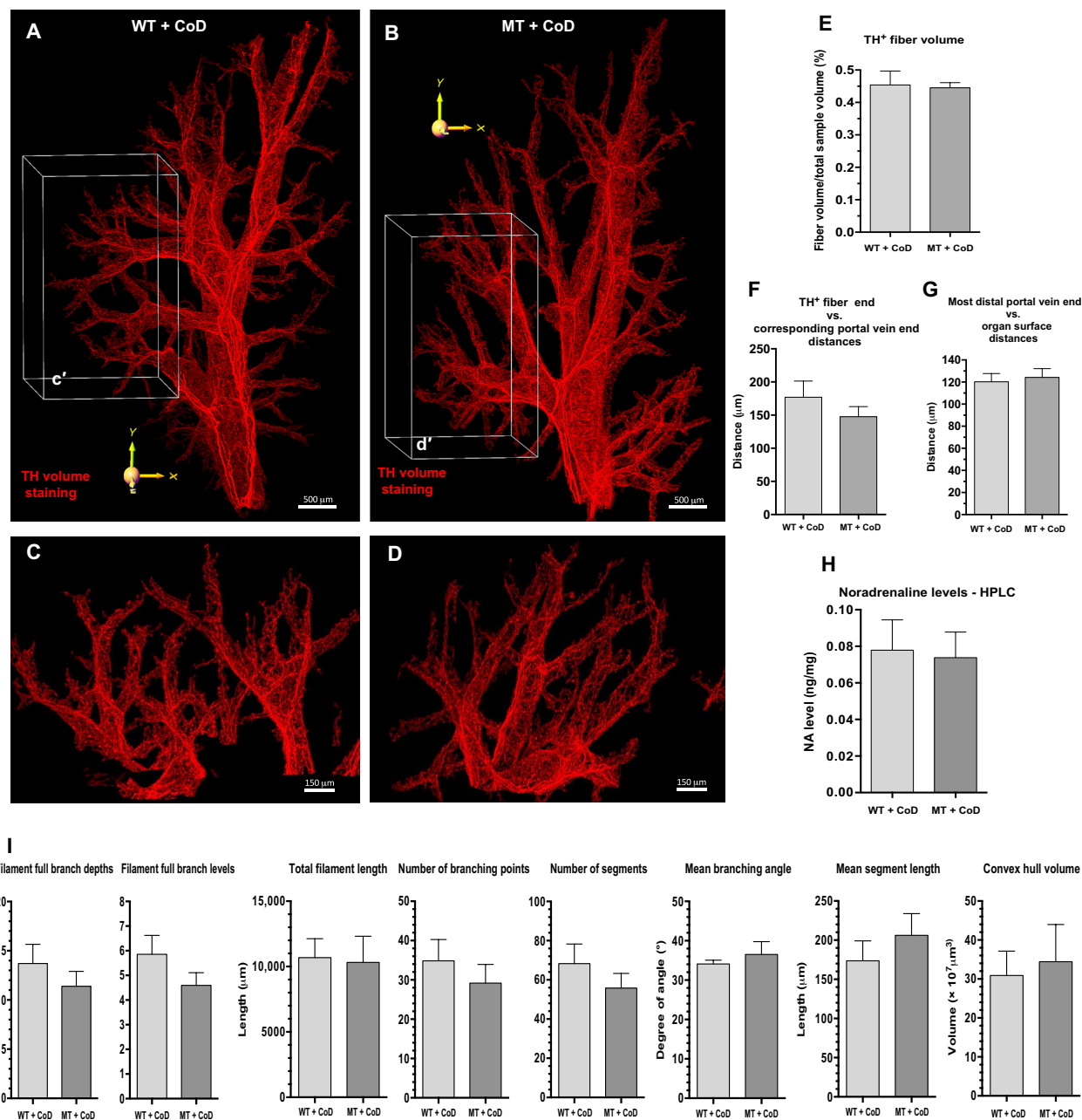
Fig. 7. SNAP-25b–deficient mice on control diet (MT + CoD) do not show signs of sympathetic axonal degeneration. (**A** to **D**) TH 3D staining of WT control diet (WT + CoD) (A and C) and SNAP-25b–deficient on control diet (MT + CoD) (B and D) samples. Boxed volumes in (A) and in (B) [(c′) and (d′), respectively] are enlarged in (C) and (D), respectively. (**E**) Quantification of total sympathetic fiber volume in MT + CoD versus WT + CoD; $n = 5$ to 7 per group. (**F**) Quantification of TH⁺ fiber ending/corresponding portal vein ending distances in MT + CoD versus WT + CoD ($n = 5$ per group). (**G**) Quantification of most distal portal vein ending/organ surface distances in MT + CoD versus WT + CoD ($n = 5$ per group). (**H**) Measuring of hepatic NA levels in MT + CoD versus WT + CoD; $n = 6$ to 9 per group. (**I**) Quantified results of filament tracing in MT + CoD versus WT + CoD; $n = 5$ to 7 per group. Data expressed as means ± SEM. Scale bar is indicated in each micrograph.

central vein/portal area volume ratio was increased in the MT + WD (steatohepatitis) samples, compared to controls. In contrast, no significant change in portal area volume was noticed in the WT + WD group, nor was a change found in the morphology or total volume of central veins in any group (Fig. 9, E and F). In a more detailed analysis of the portal area, 3-mm-long main portal branches were manually segmented in each sample, and the portal vein volumes were determined (Fig. 9, G and H). This measurement revealed a

remarkable decrease in the portal vein volume of the MT + WD group, which was responsible for the volume reduction of the portal area (Fig. 9, I to K, and fig. S4, A to E).

The portal vein stenotic alteration in steatohepatitis correlates with the extension of the sympathetic innervation

We then examined the spatial relation between the sympathetic innervation and the portal vessels. Interestingly, the stenotic portal
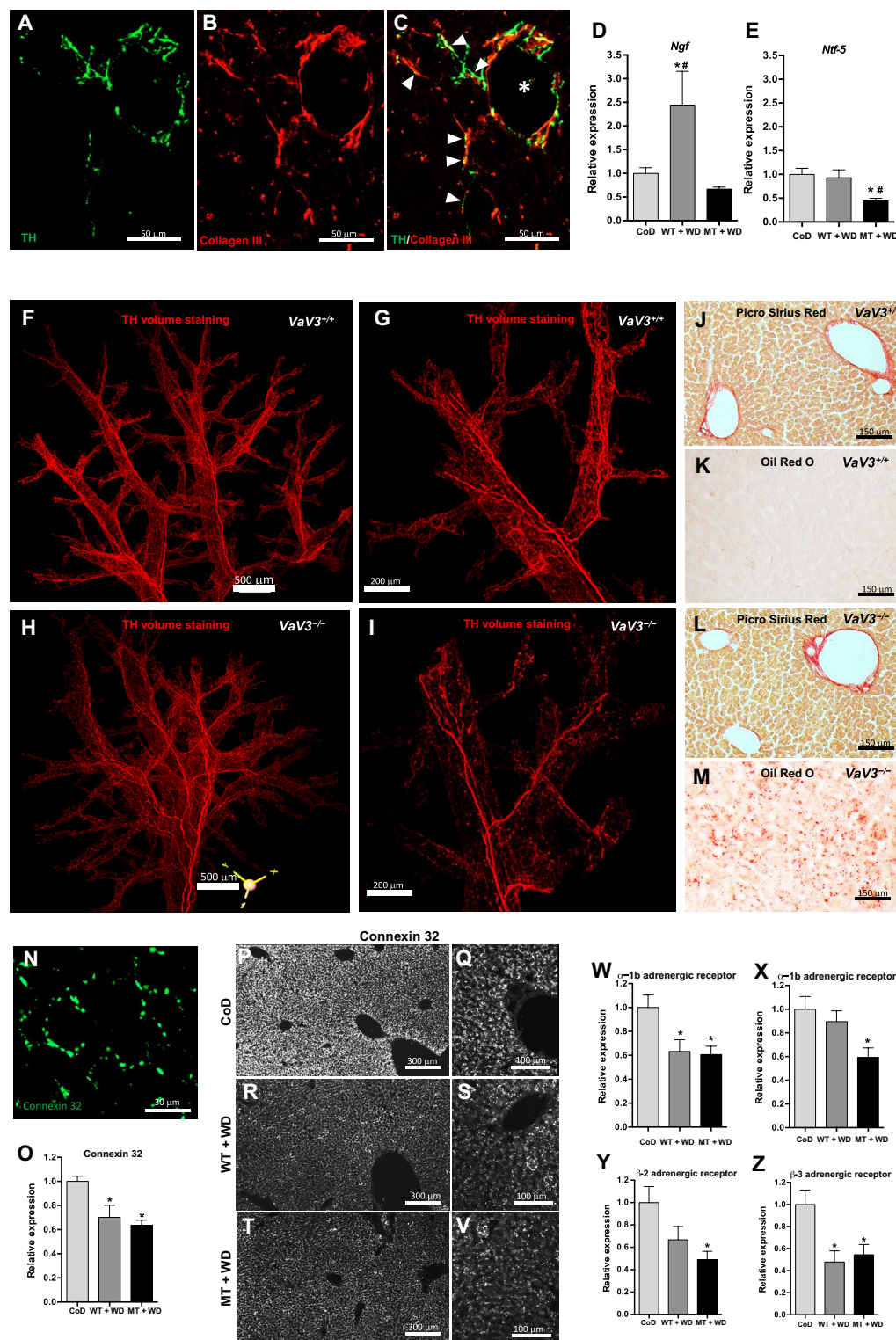
Fig. 8. Role of collagen III, growth factors, connexin 32, and adrenoreceptors in experimental steatosis/steatohepatitis. (**A** to **C**) TH + collagen III 2D costaining of WT + WD portal area. Arrowheads in (C): NAergic fibers leaving the portal area and following collagen fibers. *Portal vein. (**D** to **E**) NGF (D) and neurotrophin-5 (NTF-5) (E) mRNA expressions, qPCR. (**F** to **I**) TH 3D staining of $Vav3^{-/-}$ mouse liver (H and I) and WT controls (F and G) as overview (F and H) and zoom (G and I). (**J** to **M**) Picro Sirius Red (J and L) and ORO histochemistry (K and M) of $Vav3^{-/-}$ (L and M) and control (J and K). (**N**) High-resolution confocal image of CX32 staining from CoD. (**O**) $Cx32$ expression, qPCR. (**P** to **V**) CX32 staining of CoD (P and Q), WT + WD (R and S), and MT + WD (T and V). Overview (P, R, and T) and higher resolution (Q, S, and V). (**W** to **Z**) Adrenergic receptor expressions, qPCR. $n = 7$ to 8 per group. *$P < 0.05$, CoD versus MT + WD; #$P < 0.05$, WT + WD versus MT + WD. Data expressed as means ± SEM. Scale bar is indicated in each micrograph.
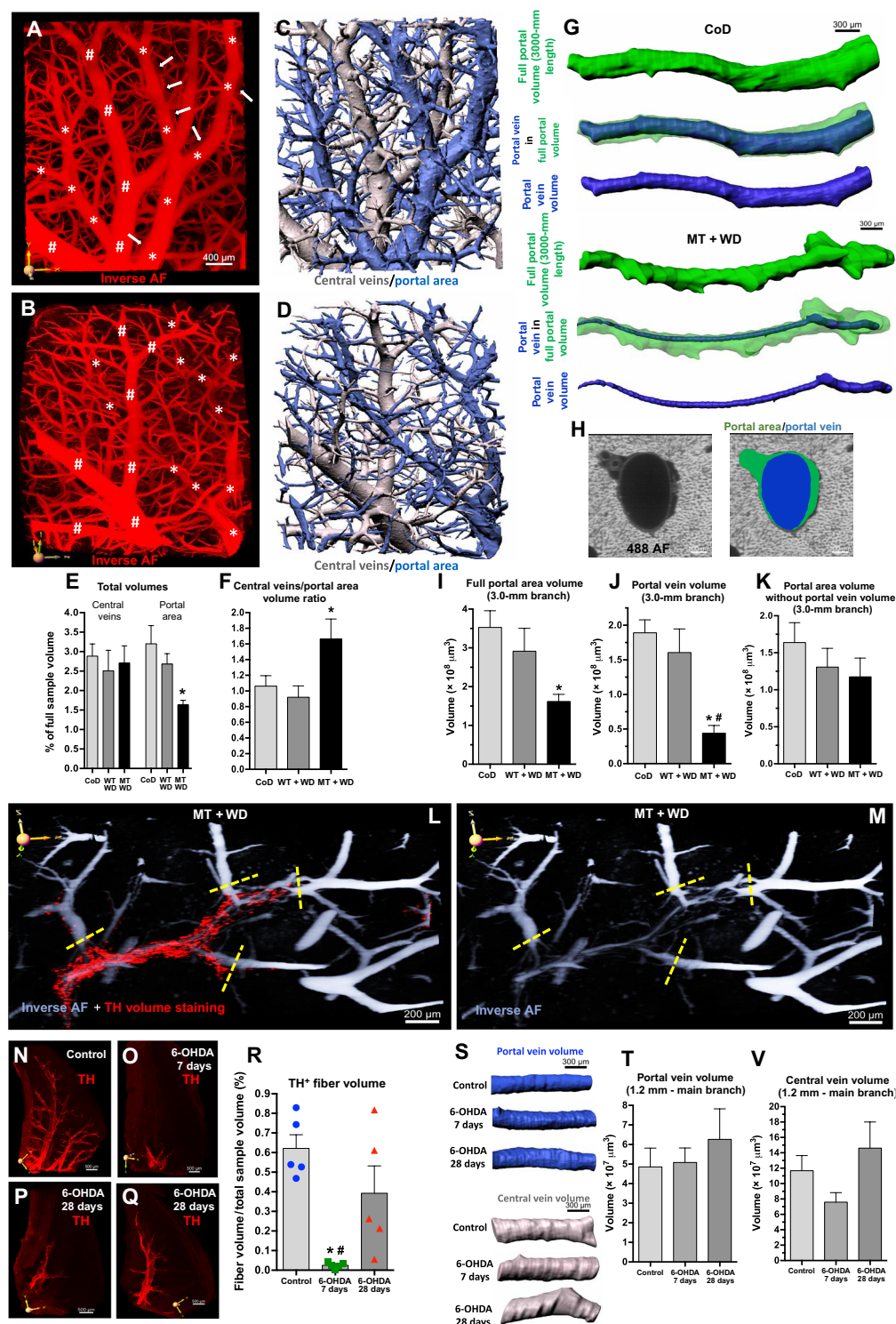
Fig. 9. Portal vein stenosis in experimental steatohepatitis and its spatial correlation with remaining sympathetic fibers. (**A** to **D**) Inverted 488 AF depicting the vasculature on CoD (A) and MT + WD (B) full samples. Segmented portal area (blue) and central veins (gray) in the same samples (C and D). *Portal area main branch; #central veins main branch. (**E** and **F**) Quantification of portal area and central veins in full samples. Total volumes (E) and central vein/portal area volume ratio (F). (**G** and **H**) Manual 3D segmentation of the portal area (green) and portal vein (blue) in 3-mm major portal branches in CoD (top) and MT + WD (bottom). Explanation on 2D optical slice (H). (**I** to **K**) Quantified volumes of portal area (I), portal vein (J), and portal area without portal vein volume (K) in 3.0-mm branches. (**L** and **M**) Inverted AF (gray) and TH 3D staining (red) in an MT + WD liver. Yellow dashed lines: end of TH⁺ innervations. (**N** to **R**) TH 3D staining on control liver (N), 7 days (O) and 28 days (P and Q) after 6-OHDA, and its quantification (R). (**S** to **V**) 3D reconstruction of portal vein (S; top) and central vein (S; bottom) in 1.2-mm branches of control, and 7 days and 28 days after 6-OHDA, and their quantifications (T and V); $n = 5$ to 6 per group. *$P < 0.05$, CoD versus MT + WD; #$P < 0.05$, WT + WD versus MT + WD. Data expressed as means ± SEM. Scale bar in (A) is for (A) to (D). For the rest, the scale bar is indicated in each micrograph.

vein alterations in the MT + WD samples exactly overlapped with the (already degenerating) NAergic innervations. Outside these regions, the more distal end parts of portal veins were again dilated (Fig. 9, L and M, and fig. S4, F to I).

Last, we tested the hypothesis that the decrease of liver sympathetic tone may cause alterations in portal vein dilation/volume. Seven days after treatment with 6-hydroxydopamine (6-OHDA; 100 mg/kg, i.p.) on control mice, the TH 3D staining was minimal with a partial recovery after 28 days, but with a high interindividual variability (Fig. 9, N to R). The portal or central vein volumes did not change significantly (Fig. 9, S to V). Overall, elimination of the sympathetic tone itself does not significantly affect the contraction state of either portal or central veins in control (nonsteatotic) mice.

Searching for sensory and parasympathetic innervations of the mouse liver
3D staining for the primary sensory nerve marker CGRP revealed sparse thick (5 to 15 μm) nerve fibers, without a fine fiber network, around the major portal branches in the quadrate left lateral lobe samples (fig. S5, O to R). No signs of pathology or apparent difference from control were noticed in steatotic/steatohepatitic samples in the 3D pattern of CGRP+ fibers (fig. S5, S and T).

Volume or 2D immunostaining for VAChT and other cholinergic markers (acetylcholinesterase, the peripheral isoform of choline-acetyl transferase, and vasoactive intestinal polypeptide) did not reveal any fiber staining (fig. S5, H to K). Also, analysis of ChAT(BAC)-eGFP transgenic mouse livers yielded negative results (fig. S5L). In contrast, these approaches showed expected fiber patterns in pancreas, muscle, and various brain regions (fig. S5, A to G, M, and N). Overall, these results suggest that the mouse liver does not contain substantial cholinergic (parasympathetic) innervation.

Processing human livers for volume imaging and pathological characterization of samples
To test the translational relevance of our mouse data, we collected human liver biopsy samples (see table S1) and processed them for TH 3D staining. Since the human liver contains abundant connective tissue and exhibits high AF, the iDISCO+ protocol was modified to optimize staining and clearing quality (see Materials and Methods). Each sample was pathologically characterized and sorted by lipid content (fig. S6, A to F). Six examined cases showed no detectable or minimum amounts of fat (#1 to 6), four moderate steatosis (#7 to 10), and four severe steatosis with remarkable inflammation and ductular reaction (#11 to 14). Two cases (#12 and #13) also exhibited marked fibrosis. The severely steatotic case #14, however, showed only mild fibrosis (fig. S6, A to F). Samples #11 to 14 were macroscopically whitish (fig. S6C) and defined as steatohepatitis.

Sympathetic innervation of the human liver in 3D
The human liver sympathetic innervation in samples with no detectable fat showed six to eight, 30- to 70-μm-thick TH+ NAergic nerve bundles running along the big portal vessels, giving rise to thinner (4- to 8-μm-diameter) fibers forming a dense network around all elements of the portal triad (Fig. 10, A, B, and F; fig. S7, A and B; and movie S4). In addition, 4- to 8-μm-thick nerve bundles, originating from the fine network around the main portal

branches, penetrated the parenchyma in the connective tissue septa around the lobuli, often following the smaller portal branches in the septa (Fig. 10, A and B, arrows). From this "interlobular innervation," 3- to 6-μm-diameter fine varicose nerve fibers penetrated the intra-lobular parenchyma with decreasing density toward zone 3 ["intralobular" innervation: Fig. 10, B (arrowheads), C to E, and fig. S7, C and D] in the perisinusoidal space (running together with fine collagen III+ fibers; Fig. 10G).

3D analysis of sympathetic nerve fibers in severe steatotic/steatohepatitic human livers reveals axon degeneration
NAergic fibers in the human liver showed a degenerative pathology in both steatosis and steatohepatitis samples, with a clearly more marked degeneration in the severe cases. In moderate-severe steatosis samples, a decreased density of intraparenchymal fine fibers was noticed with frequent swollen axonal varicosities and fragmentation of the remaining innervation. Such swollen axonal pathology was especially severe in cases #10 and #11 (Fig. 10, I versus H and O versus N, and fig. S8, B versus A). In cases #12 and #13, both with severe steatosis, inflammation, and fibrosis, the intralobular fibers were very sparse, and even the remaining ones exhibited a severe, swollen pathology. Moreover, interlobular nerve fibers also presented frequent swollen axonal varicosities (Fig. 10, J versus H; fig. S8, C versus A; and movie S5). In the severely steatotic case #14, the intra- and interlobular NAergic fibers had almost completely disappeared, and only the thick nerves around the bigger portal tracts were preserved (Fig. 10, K versus H, and fig. S8, D versus A). Last, we quantified the intralobular innervations in all cases and, in agreement with the qualitative examination, a significant decrease in the volume of intralobular, fine NAergic fibers was measured in the steatosis versus nonsteatosis samples (Fig. 10, L and M).

DISCUSSION
In the present study, we applied the novel volume immunoimaging technology iDISCO+ and light sheet microscopy to explore the integrity of hepatic innervations at various stages of NAFLD in both experimental mouse models and human tissues. TH 3D staining confirmed the periportal sympathetic innervation in mouse liver that was previously described in several studies (43, 44). In addition, the large-scale 3D reconstruction of the left lateral lobe revealed that the complex sympathetic neuronal network follows each portal branch, extending almost until the end of the most distal portal vessels. In contrast, primary sensory nerves (CGRP+) are sparse and appear only to follow larger (more proximal) portal branches. We could not detect any parasympathetic (cholinergic) nerves. The vast majority of earlier data concerning mouse liver cholinergic innervation is based on AChE histochemistry (45, 46). However, this is not a reliable and specific cholinergic staining in the liver (47). Studies applying VAChT immunohistochemistry did not find cholinergic nerves in rat (48) or mouse (49) liver. A recent volume imaging study also failed to detect cholinergic innervations in the mouse, rhesus macaque monkey, and human liver (50). Moreover, studies applying hepatic vagotomy and reporting its physiological consequences may be taken with caution, since hepatic parasympathetic denervation actually lesions the common hepatic vagus branch, including also the gastroduodenal branch that innervates parts of the distal stomach, pylorus, duodenum, and pancreas (51, 52). Some authors speculate that the vagal nerve indirectly controls liver
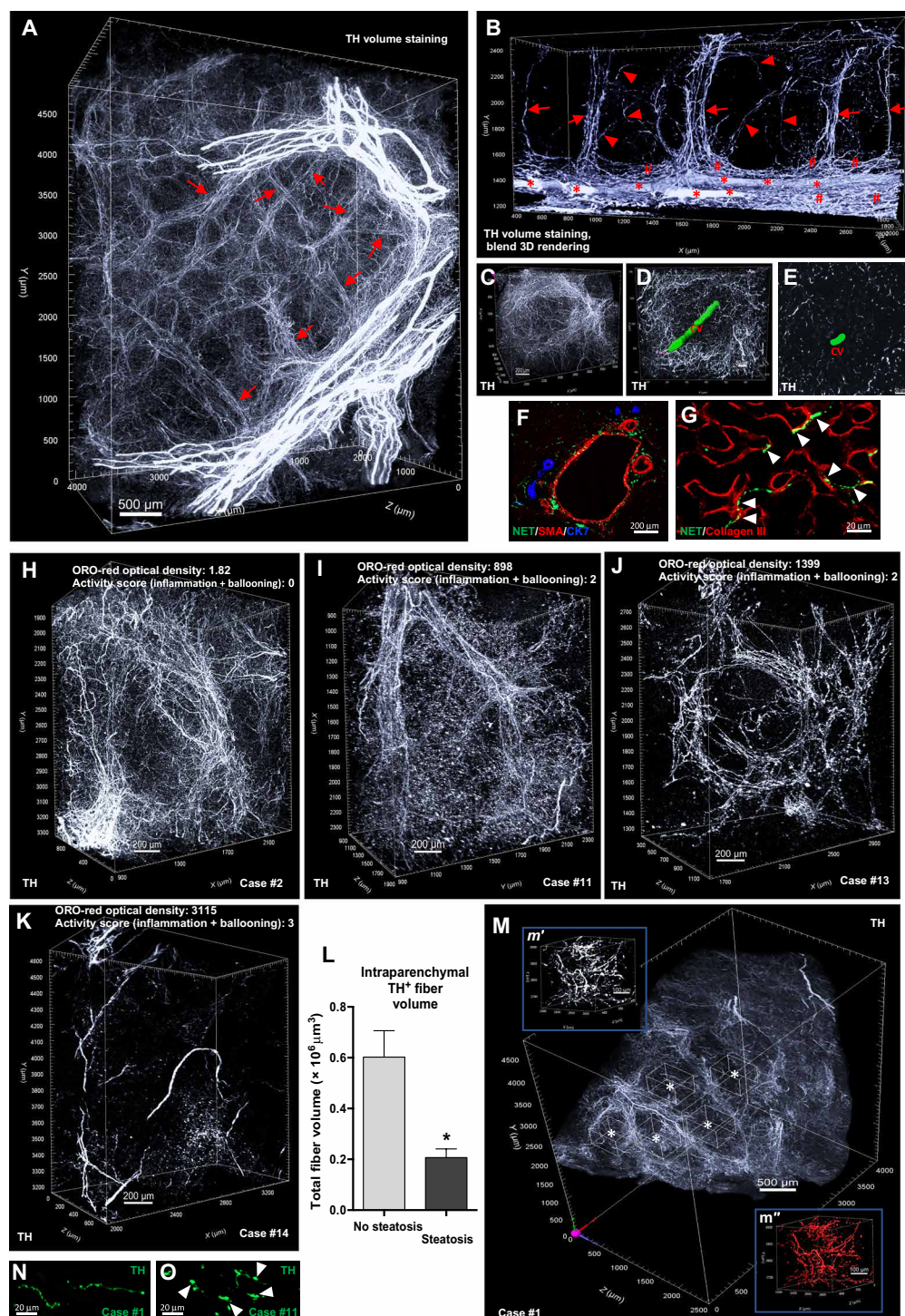
Fig. 10. Sympathetic innervation of the human liver and its degeneration in severe steatosis/steatohepatitis. (A and **B)** TH 3D staining in nonsteatotic human liver sample. Full sample (A); zoom, blend 3D-rendering mode (B). Arrows: interlobular branches; arrowheads: intralobular fine fibers; *major thick nerves; #fine fiber network around the main portal vessels. (**C** to **E)** TH 3D staining, zoom of a lobulus. 3D rendering (C), central vein (CV, green) is segmented (D), 2D optical slice from (C) (E). (**F)** Norepinephrine transporter (NET), αSMA, and CK7 triple staining, nonsteatotic liver, portal area. (**G)** NET + collagen III double staining, intralobular parenchyma, non-steatotic liver. Arrowheads: fine nerve fibers running along with collagen fibers. (**H** to **K)** TH 3D staining of samples sorted by increasing lipid content. Full samples are shown in fig. S8. (**L)** Quantification of the fine intralobular NAergic fiber volume. "No steatosis"= 0 in steatosis score, "steatosis"= 1 to 3 in steatosis score; cf., fig. S6B. (**M)** Sampling of the fine intralobular fiber volume for quantification. Details are in the Supplementary Materials ("3D quantification processes and algorithms applied on light sheet microscopy scans" section). *Virtual rectangles for sampling; m': 3D cropped virtual rectangle with TH 3D staining; m'': surface created based on the 3D staining shown in m'. (**N** and **O)** Fine intralobular NAergic fibers, high-power confocal images in nonsteatotic liver (N) and in steatohepatitis (O). Arrowheads: swollen varicosities/ intervaricose connections. *$P < 0.05$. Data expressed as means ± SEM. Scale bar is indicated in each micrograph.

functions by affecting the celiac (sympathetic) ganglion or microganglia near the celiac artery (53). Overall, our volume imaging study supports the notion that there is no relevant amount of cholinergic nerves in the mouse liver. Nevertheless, a limited cholinergic innervation, e.g., around the hilus, cannot be excluded; further research is needed to address this specific question.

One major goal of the present study was to explore the integrity of the hepatic nerve supply in experimental NAFLD. We hypothesized that the reported chronic sympathetic overactivation, steatosis, and proinflammatory and profibrotic environment in the fatty liver may cause pathological alterations in the innervation of the organ. A 7-week WD resulted in a moderate steatosis and mild inflammation without significant fibrosis or ductular proliferation in control mouse liver. However, a detailed 3D analysis of the NAergic fibers of these animals revealed widespread enlarged/swollen axonal varicosities in the fine filaments, mild fiber retraction in the most distal nerve branches, and frequent abnormal axonal sprouting extending from the Glisson's capsule into the parenchyma in the more proximal branches.

We and others have shown swollen axonal pathology (i.e., enlarged/swollen varicosities/intervaricose connections) in nonmyelinated monoaminergic axons in the CNS in aging or in various pathological conditions (32–34, 54, 55). Such pathological derange is generated by accumulation of intra-axonal materials due to destabilization of microtubules and impaired axonal transport (55, 56). In fatty livers, increased oxidative stress in the NAergic fibers caused by chronically high nerve activity (14) or by reactive oxidative species derived from lipid-laden injured hepatocytes (4) or from infiltrating neutrophil granulocytes as a part of inflammation processes (7) may all contribute to the axonal pathology. We show here that 4-month-old $Vav3^{-/-}$ mice characterized by chronic sympatho-excitation and fatty liver (13) also exhibit swollen axonal pathology. Together, a chronically high sympathetic tone may contribute to the development of nerve pathology in hepatic NAergic fibers, and our results further support a pathological link between liver sympathetic nerve dysfunction and liver steatosis.

In the WT + WD mice, NGF expression is increased, paralleled by NAergic fiber sprouting toward the liver parenchyma. Ectopic NGF expression is efficient in rearranging intrahepatic nerves, where extension of nerve fibers from the periportal area toward the pericentral area is induced (39), similar to what we observed in our steatosis model. The increased NGF expression and sprouting may be a physiological compensatory response to the distal axonal atrophy. In addition, the reorganization of the ECM in fatty liver may also destabilize the nerve fiber network. Namely, ECM proteins such as collagens I and III provide mechanical support for axons/axonal growth (57, 58), and molecular reorganization of ECM matrix is an early event in the development of fibrosis (37, 38). We showed here that NAergic filaments in the liver run along collagen fibers. The destabilization of ECM–nerve fiber connections may lead to disorganization of fine periportal nerve filaments and may initiate increased NGF expression and axonal sprouting. This sprouting is, however, apparently limited to a few hundred micrometers toward the parenchyma, perhaps due to an inefficient/abnormal ECM support. Overall, volume imaging revealed that disorganization/signs of mild degeneration and axonal sprouting/increased nerve plasticity are simultaneously detectable in the mouse liver sympathetic innervation in steatosis in experimental NAFLD.

$SNAP$-$25b$–deficient mice kept for 7 weeks on WD exhibit diabesity. Altered feeding behavior and hypothalamic dysfunction (36), as well as impaired beta-cell and islet functions, may be its primary cause (59). These mice also show severe liver steatosis and inflammation, indications for hepatocellular injury (ballooning), fibrosis, and ductular reaction, a liver status that corresponds to advanced steatohepatitis. Our 3D analysis allowed a detailed quantitative characterization of a sympathetic nerve degeneration in these mice, demonstrating complete disappearance of distal branches and severe swelling of remaining axonal varicosities/intervaricose connections. In addition, decreased levels of NA and galanin were observed. This nerve pathology is more advanced and aggravated as compared to the "steatosis" stage in WT mice on WD and presumably associated with functional impairment. In these steatohepatitic livers, no proximal sprouting or increase in NGF expressions is detected; the NAergic innervation is apparently collapsing. After submission of the present work, a paper was published where the authors describe liver sympathetic neuropathy in mice kept on a 20- to 24-week high-fat diet as well as in 12-week-old ob/ob and db/db mice, applying volume imaging technology (50). While this study of Liu et al. (50) lacks detailed qualitative or quantitative characterization of the fiber dystrophy and its comparison with the hepatic NAFLD spectrum pathology, the authors demonstrate, with a series of elegant experiments, that the noticed fiber damage can be reversed by calorie restriction or neutralizing TNFα antibody treatment in mice previously fed with a high-fat diet or by recombinant leptin treatment of ob/ob mice.

We demonstrate that the periportal NAergic fibers in mouse liver form close contacts with vascular smooth muscle and endothelial cells, as well as with biliary epithelial cells. All these cells express adrenergic receptors (19, 42, 60). Because of the limited innervation in mice and rats, hepatic gap junctions play a crucial role in the signal propagation throughout the parenchyma following sympathetic stimulation (40, 41). Here, we describe decreased expression of α1b and β3 adrenergic receptors and $Cx32$, the major component of mouse liver gap junctions, already at the steatosis level (WT + WD mice). These changes may represent a physiological response to a chronically high sympathetic nerve tone. The decreased expression levels of adrenergic receptors and $Cx32$ were even more pronounced in steatohepatitis (MT + WD), which, together with the nerve degeneration, suggests that the entire intrahepatic sympathetic nerve-mediated communication is impaired in these livers. In contrast, the limited CGRP+ primary sensory innervation, which has an otherwise important role in nutrient (including glucose and lipid) sensing around the portal vein (52), does not exhibit any morphological signs of degeneration.

Since the sympathetic innervation of human liver is much more complex than in rodents (44), it is important to test the translational relevance of our mouse data by also investigating human livers. Human liver sympathetic innervation was previously studied earlier in 2D (43, 47, 61). Here, we show that volume imaging allows, in an unparalleled way, a comparative analysis. Current available data concerning changes in human liver innervation in pathological conditions are sparse. Earlier studies applying S100 and/or neuron-specific enolase immunostaining described a decrease of intraparenchymal nerve fiber density in cirrhosis and increased hepatic innervations in hepatitis (21–25, 62). However, these studies do not focus on earlier stages of NAFLD, and the applied markers do not discriminate between sympathetic and other types of nerves. Here, we examined the sympathetic innervation of liver samples with

volume imaging from 14 subjects ranging from undetectable steatosis to severe steatohepatitis. Samples with liver pathology other than NAFLD spectrum were excluded.

Thin intralobular NAergic fibers in the Disse space exhibit distinct changes already in moderate steatosis, which become more severe in steatohepatitis, reaching the interlobular fibers. Reasonably, the nerve pathology starts in the thin unmyelinated and often unsheathed intralobular, most distal fibers (63) that form neuro-effector junctions with hepatocytes, stellate cells, sinus endothelial cells, and Kuppfer cells (47, 64). These terminal fibers are probably particularly exposed and vulnerable to oxidative stress. With more advanced stages of NAFLD, the pathology spreads to the thicker interlobular fibers. Even if it is more complex in human, the nerve fiber pathology detected in human NAFLD is largely similar to what was observed in the mouse model. The decrease of intralobular fine fiber volume is detectable already in human samples with moderate steatosis, which supports the notion that the developing steatosis and subsequent lipotoxicity may be a key factor in the sympathetic nerve pathology. At the same time, a more widespread degeneration is noticed only in steatohepatitic livers, indicating that steatosis and inflammation together may cause severe nerve damage. Last, it is interesting to note that the most severe nerve degeneration was detected in a liver with heavy steatosis and severe inflammation but without substantial fibrosis, suggesting that fibrosis per se may not be the ultimate determinant in the development of sympathetic nerve degeneration in human NAFLD.

Supraphysiological pressure in the portal venous system, called portal hypertension (PH), is a detrimental complication in liver cirrhosis (65). The pathophysiology of PH is complex, involving hepatic (increased intrahepatic resistance to portal venous blood flow due to tissue remodeling) and/or extrahepatic (splanchnic arterial vasodilation) factors (65, 66). Despite the fact that PH has mostly been discussed in the context of cirrhosis, elevated portal venous pressure has also been detected in experimental or human NAFLD, when fibrosis was less advanced and cirrhosis was absent (66, 67). Numerous earlier studies reported decreased hepatic blood flow and increased hepatic arterial and portal venous pressure after electric stimulation of the hepatic nerves in rat (68), dog (69), or cat (70). Moreover, electrical stimulation of portal vein–associated nerves elicited α-receptor–mediated constriction of portal venules, sinusoids, and hepatic arteries, but no response could be recorded from the central vein (60). Together with the well-established chronically high sympathetic tone in NAFLD, a potential role of intrahepatic nerves also in the development of PH is suggested.

Here, we describe and quantitatively characterize a portal vein stenotic alteration in the steatohepatitic MT + WD group. Systematic 3D analysis reveals that this stenosis ends exactly where the degenerating NAergic innervation terminates, after which the more distal parts of the portal veins are again dilated. At the same time, the central vein system that virtually lacks innervation does not show decreased volume or shrunken morphology. These findings propose that the liver periportal sympathetic nerves could contribute to a stenotic portal vein condition in advanced stages of NAFLD, thus representing a potentially novel neuronal component in the patho-mechanism underlying PH.

The spatial correlation of the portal vein stenosis and the remaining NAergic fibers support the notion that these morphologically impaired nerves are still in operation, albeit presumably with impaired functionality. Notably, abolishment of the sympathetic

nerve tone with 6-OHDA treatment in healthy control mice did not change the volume of the portal veins in our study, which is in line with the earlier finding that sympathetic denervation had no significant influence on hepatic blood flow in control rats (68, 71). Thus, sympathetic nerves may only exert a modest tonic influence on hepatic blood flow in normal conditions.

Our study has several limitations. First, we studied only 4-month-old $Vav3^{-/-}$ mice, and SNAP-25b–deficient mice and WT littermates on 7 weeks of WD. To explore the causal relationship of chronic sympathetic overactivation, sympathetic fiber pathology, and liver steatosis/steatohepatitis in more detail, further longitudinal studies are needed to examine animals of different ages and with a time course of WD. Also, the application of gene-targeted animal models in general has substantial limitations in metabolic research, and the analysis of more physiological NAFLD models is necessary, such as control mice on extended high-fat, high-fructose diet or on extended WD. More specifically, albeit our experiments concluded that SNAP-25b deficiency per se does not affect the integrity of the liver sympathetic nerves, we cannot totally exclude the possibility that during WD (under metabolic challenge), the SNAP-25b–deficient condition might contribute to the increased vulnerability of the hepatic NAergic innervation. At the same time, our data on human livers provide translational relevance of the results with experimental NAFLD, and a recently published paper (50) also supports the presence of sympathetic nerve atrophy in the mouse fatty liver.

In summary, taking advantage of the state-of-the-art volume imaging technology, we here describe and characterize marked disturbances of the sympathetic nerves in steatotic mouse liver and a severe and selective degeneration of the same sympathetic neuronal network in steatohepatitis. Despite the anatomical differences between human and rodent liver innervations, human fatty livers show similar degeneration of sympathetic nerve fibers. Moreover, its severity correlates with the level of NAFLD pathology, supporting the translational relevance of our work and the validity of experimental NAFLD mouse models in studies of liver innervation. Nerves in the liver have multiple subtle regulatory roles in glucose and lipid metabolism, bile secretion, inflammatory reaction, hemodynamics, and regeneration. However, their role may be more essential during the fight-or-flight response or when subjected to metabolic challenges (51). Gradual atrophy of liver sympathetic nerves and abnormal operation of the remaining arborization in NAFLD could compromise all these functions, which may contribute to further aggravation of the disease, as part of a vicious cycle. Our study revealed molecular and subtle morphological alterations in the liver sympathetic innervation already in early stages of NAFLD, which can be interpreted as compensatory mechanisms and which lead to increased plasticity of the sympathetic nerve system. With progression to steatohepatitis, however, this condition turns to a severe degeneration of the nerves. Combination of 3D immunoimaging and molecular methods may help to understand better how simple steatosis develops to steatohepatitis and may open up new important therapeutic approaches in NAFLD in the future. Last, our present study provides a powerful approach and workflow to comprehensively study liver nerves, vasculature, and/or bile ducts, even simultaneously, at high resolution and in 3D, in experimental animal models and in human tissue. Considering the increasing body of evidence regarding the importance of the hepatic innervation, our novel approach contributes to new insights into liver biology.

MATERIALS AND METHODS

Gene-targeted and transgenic mouse lines [*SNAP-25b*–deficient, *ChAT(BAC)-eGFP*, and *Vav3*$^{-/-}$]

The generation, breeding, maintenance, and genotyping of *SNAP-25b*–deficient mice and *ChAT(BAC)-eGFP* transgenic mice, both backcrossed on C57BL/6Crl, were performed as previously described (*72*, *73*). In the *SNAP-25b*-deficient line, total expression levels of SNAP-25 proteins did not change, but only SNAP-25a is expressed (*72*). MT mice and WT littermates were maintained at the animal facility of Karolinska Hospital and housed six per cage in an environmentally controlled room (22° to 24°C) under a regular 12-hour light/12-hour dark cycle (lights on 7:00 a.m.) with food and water ad libitum. All experimental procedures were performed on male mice, between 9:00 a.m. and 2:00 p.m., under Ethical Permit #N33/14 approved by the Stockholm Northern Animal Experiments Ethics Board, and were performed according to standards and guidelines in accordance with the Directive 2010/63/EU of the European Parliament and of the Council on the Protection of Animals Used for Scientific Purposes. Particular care was taken to minimize the number of animals and their suffering throughout the experiments.

Vav3$^{-/-}$ *C57BL/10* mice with chronic sympathetic hyperactivity were generated, bred, maintained, and genotyped as described earlier (*74*, *75*). The Cincinnati Children's Hospital Medical Center Institutional Animal Care and Use Committee approved the protocol.

Human liver biopsy samples

Together, 21 human liver biopsies were collected, but seven were excluded from the study based on clinical data and pathological evaluations (one infant, one with suboptimal fixation, one with genetic metabolic disorder affecting the liver, one portal vein–embolized subject, and three subjects with hepatitis without steatosis). The clinical data of the applied subjects are reported in table S1. If the indication for surgery was a liver tumor, the sample used was taken from the healthy (nontumorous) tissue part of the organ. The results of the pathological evaluation for the 14 involved cases are summarized in fig. S6. All procedures were approved by the Regional Committee of Science and Research Ethics (Etikprövningsmyndigheten, Uppsala, Sweden; ethical permission no: 2017/269-31 and amendment with no. 2020-00713) and were in agreement with the Declaration of Helsinki. Each involved patient provided written informed consent.

Western diet

The diet intervention started at the age of 5 weeks. Male *SNAP-25b*-deficient mice and WT littermates were divided randomly, three mice per cage, with a similar average body weight and were assigned to either (i) control diet (CoD; Lantmännen, Sweden; R70; 10.5% of kilocalories from fat, 17.7% from proteins, and 71.7% from carbohydrates) or (ii) high-fat/high-sucrose WD (Research diets Inc., New Brunswick, NJ, USA; D12079B; 40.0% of kilocalories from fat, 17.0% from proteins, and 43.0% from carbohydrates). Free-feeding animals received these diets for 7 weeks.

6-OHDA treatment on mice

The experiment was performed in male mice (strain C57Bl/6J, Charles River, Sulzfeld, Germany; average weight was 22.9 ± 0.18 g at the beginning of the experiments). Mice were housed six per cage

and were kept under controlled conditions in the animal facility (12-hour light/12-hour dark cycle, lights on at 7:00 a.m.; temperature, 22° ± 2°C; humidity, 55 ± 10%) with free access to tap water and standard pelleted chow. All experimental procedures were performed between 8:00 a.m. and 1:00 p.m., with all external noise or any other stimuli stressful to the animals being strictly avoided. All experimental procedures were approved by the Animal Care Committee of the Institute of Experimental Endocrinology, Biomedical Research Center, Slovak Academy of Sciences, Bratislava, Slovakia and State Veterinary and Food Administration of the Slovak Republic (Approval No. Ro 1314/18-221). The mice received care in compliance with the *Guide for the Care and Use of Laboratory Animals* published by the U.S. National Institutes of Health.

Mice were randomly divided into four experimental groups: (i) control mice with intact sympathetic nervous system euthanized 7 days after vehicle injection (VEH 7; *n* = 3); (ii) control mice with intact sympathetic nervous system euthanized 28 days after vehicle injection (VEH 28; *n* = 3); (iii) sympathectomized mice euthanized 7 days after neurotoxin injection (6-OHDA 7; *n* = 6); and (iv) sympathectomized mice euthanized 28 days after neurotoxin injection (6-OHDA 7; *n* = 6).

Chemical sympathectomy was carried out in 12 mice by intraperitoneal injection of the neurotoxin 6-OHDA hydrobromide [body weight (100 mg/kg), Sigma-Aldrich, Darmstadt, Germany] in conscious mice over two consecutive days as was previously described (*76*). Briefly, the 6-OHDA was dissolved in a solution of sterile saline containing 0.1% of the antioxidant ascorbic acid (Sigma-Aldrich). Mice of the VEH 7 and VEH 28 groups were intraperitoneally injected with vehicle (solution of sterile saline containing 0.1% of the antioxidant ascorbic acid). The efficiency of the sympathectomy was confirmed in the sympathectomized mice immediately after application of 6-OHDA by the presence of ptosis (Claude Bernard–Horner's syndrome), as well as the presence of reddish urine indicating the presence of 6-OHDA metabolites in urine.

Mouse tissue preparation

For morphological examinations (iDISCO+ volume imaging and histochemical and immunohistochemical staining), mice were deeply anesthetized using sodium pentobarbital (60 mg/kg, i.p.). They were perfused via the ascending aorta with 40 ml of Tyrode's buffer (37°C), followed by 20 ml of warm modified Zamboni fixative (mixture of 4% paraformaldehyde and 0.2% picric acid, diluted in phosphate buffer, pH 7.4) and 50 ml of the same fixative at 4°C. The entire livers were dissected out and postfixed in the same fixative for 3 hours at 4°C. The left lateral lobe planned for volume imaging was then immersed and kept in 1× phosphate-buffered saline (PBS; pH 7.4; Ambion), containing 0.1% sodium azide, pending analysis. Another piece of liver was reserved for histochemistry and immunohistochemistry and was immersed in 10% sucrose in PBS (pH 7.4), containing 0.01% sodium azide (Sigma-Aldrich) and 0.02% bacitracin (Sigma-Aldrich), for 48 hours. Tissue blocks were then snap-frozen with CO_2 and sectioned at 20 μm in a cryostat (Microm, Heidelberg, Germany). The sections were mounted on SuperFrost Plus slides (VWR international, Leuven, Belgium). In some animals, brains, pancreas, and soleus muscles were also dissected and further processed for 3D and 2D morphological examination.

For biochemical examinations [HPLC, radioimmunoassay, and quantitative polymerase chain reaction (qPCR)], mice were decapitated,

and the livers were rapidly dissected out. The left lateral lobes were further dissected to four pieces, following the scheme in Fig. 1B. All pieces were collected in separated Eppendorf tubes, quickly frozen on dry ice, and kept at −80°C, pending analysis.

A few animals from each treatment group were decapitated, and the livers were fixed by immersion in modified Zamboni fixative for 72 hours at 4°C, washed in 1× PBS, put into 70% ethanol, and routinely processed and paraffin-embedded. Four-micrometer sections were cut on a rotary microtome (Microm HM355s, Thermo Fisher Scientific), and sections from each block were routinely stained with hematoxylin-eosin.

Human tissue preparation and pathological characterization
Approximately 1-cm^3 human liver biopsy samples were washed in warm 1× PBS and were fixed by immersion in modified Zamboni fixative for 72 h at 4°C right after the surgical removal. Most of the tissue from each block was reserved for later volume imaging. After fixation, these tissue pieces were then immersed and kept in 1× PBS, containing 0.1% sodium azide, pending analysis. One smaller piece (ca. 5 mm by 5 mm by 3 mm) from each biopsy sample was reserved for histochemistry and immunohistochemistry. These pieces were cryoprotected in 10% sucrose for 48 hours, were snap-frozen with CO_2, and were sectioned at 20 μm in a cryostat, as described earlier. Another piece with the same size was transferred to 70% ethanol, routinely processed, and paraffin-embedded. Four-micrometer sections were cut on a rotary microtome (Microm HM355s, Thermo Fisher Scientific) and routinely stained with hematoxylin-eosin. Semiquantitative assessments of lipid content, inflammation status, and ballooning (activity), as well as fibrosis, were evaluated by two expert human liver pathologists, according to a widely accepted integrative histopathological algorithm scoring system (77).

ORO staining and its quantification
Frozen sections from fixed human and mouse liver tissue blocks were equilibrated for 1 hour at room temperature, washed 2 × 5 min in 1× PBS, 1 min in distilled water (DW), and 1 min in isopropyl-alcohol (IPA). Then, sections were incubated in ORO working solution for 15 min [working solution: 30 ml of stock solution and 20 ml of DW, after filtering; stock solution: 0.5% ORO dye (Sigma-Aldrich, O0625-25G) in IPA]. Sections were then immersed in 60% IPA for 10 min, in DW for 1 min, and in 1× PBS for 2 × 5 min and were mounted with coverslip using 2.5% DABCO (1,4-diazabicyclo[2.2.2]octane) in glycerol (Sigma-Aldrich).

To quantify the ORO signal in sections, three to five 1388 × 1040 pixel micrographs (mouse and human liver, respectively) were taken with 20×/0.6 objective from randomly selected regions with a Zeiss Axiophot microscope equipped with objective lenses 2.5×/0.12, 5×/0.25, 10×/0.45, and 20×/0.6, and an AxioCam HRc3 color camera, using the AxioVision 4.8 (Zeiss) software. Then, the micrographs were opened by the Image J 1.52q software and converted to 8-bit grayscale, brightness/contrast and threshold values were properly adjusted, and the "raw integrated density" (sum of values of the pixels in the image) and "area fraction" (percentage of pixels in the image) were determined.

Picro Sirius Red staining
Frozen sections from fixed human and mouse liver tissue blocks were dried for 1 hour at room temperature, washed in 1× PBS for

2 × 5 min and in DW for 1 min, and immersed in 0.1% Picro Sirius Red solution (prepared with: Sigma-Aldrich, 365548) for 15 min. Then, the sections were immersed in 0.5% acetic acid for 2 × 1 min, washed in DW for 1 min, dehydrated in 3 × 100% ethanol, and mounted with coverslip using Entellan (Merck, Darmstadt, Germany). The sections were examined and photographed in a Zeiss Axiophot microscope (see above), using 2.5×, 5×, 10×, or 20× objectives.

Immunohistochemistry with TSA+ signal amplification and fluorescence microscopy
For single immunostaining and for the first step of double/triple stainings, sections were washed in PBS and were incubated for two nights at 4°C with primary antibodies in 0.01 M (1×) PBS containing 0.3% Triton X-100, 0.02% bacitracin, and 0.01% sodium azide. (The list and specifications of all used primary antibodies are reported in table S2.) To visualize the immunoreactivity, the sections were processed using a commercial kit (PerkinElmer Life Science, Boston, MA) based on tyramide signal amplification (TSA). The sections were examined and photographed using a Nikon Eclipse E600 fluorescence microscope with objective lenses of 4×, 10×, and 20× (Nikon, Tokyo, Japan) equipped with appropriate filters and an ORCA-ER, C4742-80 digital camera using Hamamatsu Photonics Wasabi 150 software (Hamamatsu Photonics K.K., System Division, Hamamatsu City, Japan).

Double/triple immunolabeling and confocal microscopy
For double/triple labeling, immunostained sections were extensively washed in 0.01 M PBS and were incubated again for two nights at 4°C with new primary antibodies in 0.01 M PBS (table S2). After washing in 0.01 M PBS, the sections were incubated with Alexa Fluor–conjugated anti-rabbit, anti-mouse, anti-rat, anti-chicken, or anti-goat immunoglobulin G secondary antibodies (table S3) at a dilution of 1:500 in 0.01 M PBS for 2 hours. Sections were mounted with coverslip using 2.5% DABCO in glycerol (Sigma-Aldrich) and examined with a Zeiss LSM 800 airy confocal-system installed on a Zeiss Axio Observer Z1 microscope equipped with 5×/0.25, 10×/0.3, 20×/0.8, and 63×/1.4 objectives; 488-, 561-, and 640-nm lasers; and appropriate emission filters. Digital images from the microscopy were slightly modified to optimize for brightness and contrast using ZEN Lite 2.3 (blue edition; Carl Zeiss Microimaging GmbH, Jena, Germany) and Adobe Photoshop CS6 software (Adobe Systems, San Jose, CA), to best represent the immunohistochemistry observed at the microscope.

Quantification of macrophage density and inflammatory foci
To quantify the density of macrophages in mouse liver sections, F4/80 and Iba-1 immunostaining were applied. Three micrographs were taken from each section from randomly selected regions, using a Nikon Eclipse E600 fluorescence microscope with 20× objective, an ORCA-ER C4742-80 digital camera and the Hamamatsu Photonics Wasabi 150 software (details above). Then, the micrographs were opened by the Image J 1.52q software, brightness/contrast and threshold values were properly adjusted, and the raw integrated density (sum of values of the pixels in the image) and area fraction (percentage of pixels in the image) were determined.

To determine the number of inflammatory foci, sections double-immunostained for F4/80 + myeloperoxidase (MPO; neutrophil granulocyte marker) were captured on a Vslide slide scanning microscope (Metasystems, Alltlussheim, Germany) with 10× objective and

filter sets for fluorescein isothiocyanate (FITC; EX493/16–EM527/30) and Cy3 (EX546/10–EM580/30). Whole microscope slides were scanned at 2.5×, and tissue was detected on the basis of the FITC signal. After generating a position map, entire liver sections were scanned using 10× objective and FITC and Cy3 filters for F4/80 and MPO staining, respectively. Individual fields of view images were stitched, and images with high resolution were extracted (35,000 × 20,000 pixels). The large stitched files were further managed by the MetaViewer software (version V2.0104.3; Meta System GmbH). To count the inflammatory foci, the area of the entire sections was outlined, and the full section areas (μm^2, converted to mm^2) were determined for each case. The average outlined area was 21.65 mm^2 per section. The brightness/contrast of pictures was slightly adjusted, and the number of inflammatory foci (clusters of F4/80 and MPO positive cells; Fig. 3H) was determined on screen by the same observer. The treatment groups/animal numbers were coded and were unknown by the observer during the counting process.

iDISCO+ volume immunostaining on mouse and human liver samples

A total of 57 mice were processed for volume immunostaining [5 *SNAP-25b*–deficient on normal chow (control) diet, MT + CoD; 8 + 5 *SNAP-25b* WT littermate on control diet, WT + CoD; 7 *SNAP-25b* WT on WD (WT + WD); 6 *SNAP-25b*–deficient on WD (MT + WD); 5 controls for 6-OHDA experiment; 5 6-OHDA 7 days; 5 6-OHDA 28 days; 4 *Vav*$^{+/+}$; 4 *Vav*$^{-/-}$; and 3 *ChAT(BAC)-eGFP* mice]. The left lateral lobe of each mouse liver was dissected further into four equal pieces, according to the scheme shown in Fig. 1B, and these pieces (ca. 5 mm by 5 mm by 4 mm) were further processed for volume imaging experiments. In addition, in the case of *ChAT(BAC)-eGFP* mice, the soleus muscle was also removed and studied. For some WT + CoD (control) mice, the entire left lateral lobe, as one sample, was processed for volume imaging.

iDISCO+ volume immunostaining and clearing processes of mouse liver samples were performed as described earlier (*78*). Briefly, the samples were washed in 0.01 M (1×) PBS three times in 5-ml Eppendorf tubes and then were dehydrated in rinsing methanol/water series (20%-40%-60%-80%-100%-100%), 1 hour each. The samples were bleached with 5% hydrogen peroxide in 100% methanol overnight at +4°C. Then, they were rehydrated in downgrading serials of methanol/water (80%-60%-40%-20%-PBS), incubated in permeabilization solution for 2 days and then in blocking solution for 2 days, both at 37°C [0.2% Triton X-100/20% dimethyl sulfoxide (DMSO)/0.3 M glycine in 0.01 M PBS + 0.02% sodium azide, 0.2% Triton X-100/10% DMSO/6% normal donkey serum in 0.01 M PBS + 0.02% sodium azide, permeabilization and blocking solutions, respectively]. The samples were then incubated with primary antibodies or mixtures of primary antibodies (table S2) for 5 days at 37°C [antibody diluent: 0.2% Tween-20/heparin (10 μg/ml)/5% DMSO/3% normal donkey serum in 0.01 M PBS + 0.02% sodium azide]. After extensive washing overnight, the blocks were incubated in secondary antibody or mixtures of appropriate secondary antibodies (table S3) for another 5 days [diluent: 0.2% Tween-20/heparin (10 μg/ml)/3% normal donkey serum in 0.01 M PBS + 0.02% sodium azide]. Then, the blocks were dehydrated in rinsing methanol/water series (see above), incubated in 66% dichloromethane/33% methanol for 3 hours and in 100% dichloromethane for 2 × 30 min, transferred to tubes filled with 100% dibenzyl ether, and were stored in this solution.

Regarding the human liver, typically 5 mm by 5 mm by 2 mm tissue samples were cut for volume immunostaining. The samples were washed 3× in 0.01 M PBS and processed for iDISCO+ reaction as it was described for mouse tissue above, but with some modifications: (i) Before H_2O_2 bleaching, samples were incubated overnight in 66% dichloromethane/33% methanol and washed 2 × 1 hour in 100% methanol, for more extensive delipidation; (ii) the permeabilization step was applied for 4 to 5 days; and (iii) both the primary and the secondary antibody incubation steps were extended to 14 days.

Light sheet fluorescence microscopy and 3D image reconstruction

A light sheet microscope (Ultramicroscope II, Lavision Biotec, Bielefeld, Germany) and the ImSpector 347 software were used. The microscope was equipped with an Olympus 2×/0.5 objective lens, an Olympus MVX-10 0.63 to 6.3× zoom body, a 6.5-mm working distance spherical aberration–corrected dipping cap, an sCMOS (semiconductor complementary metal oxide semiconductors) camera (Andor Neo; pixel size: 2560 × 2160), and Coherent OBIS lasers (488-100 LX, 488 nm; 561-100 LS, 561 nm; 640-100 LX, 640 nm) with appropriate filters. Detailed scanning parameters for various blocks are reported in the Supplementary Materials. The serials of 16-bit uncompressed tif images (ca. 2000 to 2500 Z-levels, ca. 20 GB; raw data) were then converted to an IMS file, using the Imaris File Converter 8.4.2 or 9.2.1 programs (Bitplane, UK), and the 3D vision of acquisitions was reconstructed in the Imaris 8.4.2 or 9.2.1 (Bitplane, UK). For the illustrations, snapshot images (1200 dpi) were taken from the actual light sheet scans in perspective mode (Imaris). Background subtraction (Imaris) was routinely used for the light sheet scans, and brightness/contrast was slightly adjusted for the snapshots using Photoshop CS6.

HPLC measurement for liver NA content

Dissected and weighed tissue samples (average sample wet weight: 80.08 mg) were mixed at a ratio of 1:10 (w/v) with 0.2 M perchloric acid including 100 μM EDTA-2Na and homogenized at 0°C in a glass-pestle microhomogenizer. After standing for 30 min on ice, the homogenates were centrifuged for 15 min at 3000*g* at 4°C. The supernatants were carefully aspirated and mixed with 0.4 M Na-acetate buffer (pH 3) at a ratio of 5:1 (v/v) and filtered through a 0.22-μm centrifugal filter for 4 min at 14,000*g* at 4°C. The filtrates were stored at −80°C before HPLC analysis.

NA was determined by HPLC with electrochemical detection following minor modifications, as described elsewhere (*79*). Briefly, the HPLC System (HTEC-500, Eicom, Kyoto, Japan) included a degasser, a microflow pump, and an electrochemical detector. The potential of the glassy carbon working electrode was set to +450 mV versus the Ag/AgCl reference electrode. The supernatant or the standard was injected by using a CMA/200 Refrigerated Microsampler (CMA Microdialysis, Stockholm, Sweden) equipped with 20-μl loop and operating at +4°C. The separation was achieved on a 200 mm by 2.0 mm I.D. Eicompak CAX column (Eicom, Kyoto, Japan). The mobile phase was a mixture of methanol and 0.1 M phosphate buffer (pH 6.0) (30:70, v/v) containing 40 mM potassium chloride and 0.13 mM EDTA-2Na. The data were recorded and integrated using a computerized data acquisition system clarity (DataApex, Prague, Czech Republic). The limit of detection (defined as signal-to-noise ratio > 2) was 0.55 fmol/15 μl.

Radioimmunoassay for galanin peptide in mouse liver

Mouse liver galanin (1 to 29) was analyzed using antiserum RatGala4 raised against conjugated synthetic rat galanin as described before (80). Briefly, galanin (1-29) was labeled using the chloramine-T method, followed by purification on a reverse-phase (C18) column using a 20 to 50% gradient of acetonitrile in water with 0.1% trifluoro-acetic acid. The RatGala4 antiserum does not cross-react with neurokinin A, neuropeptide K, substance P, neurokinin B, NPY, gastrin, pancreatic polypeptide, glucagon, or NT. HPLC-purified ^{125}I rat galanin was used as radioligand and rat galanin was used as standard. The detection limit of the assay was 5 pM. Intra- and interassay coefficients of variation were 6 and 10%, respectively.

Liver RNA extraction and quantitative PCR

Total RNA was extracted using the RNeasy Plus Mini Kit (Qiagen, Dusseldorf, Germany). RNA integrity was controlled on QIAExcel (Qiagen), and concentration was measured by using Qubit (Applied Biosystems) and NanoDrop (Thermo Fisher Scientific, Massachusetts, USA). Two micrograms of RNA was reverse-transcribed using the High-Capacity cDNA Reverse Transcription Kit (Applied Biosystems, Carlsbad, CA, USA). Five nanograms of cDNA was used for real-time quantitative PCR by using primers specific for the different markers (see table S4) and Maxima SYBR green qPCR master mix (Thermo Fisher Scientific) on an Applied Biosystems 7000 Real-Time PCR System. Relative fold changes were calculated using the comparative CT method ($2^{-\Delta\Delta CT}$).

Statistical analyses

Student's t test for independent samples was applied for the evaluation of fine intralobular TH$^+$ immunostaining volume measurements in human livers. Two-way analysis of variance (ANOVA) and Tukey's post hoc tests were used for the detailed evaluation of branching angles in mouse liver major filaments. For the statistical evaluation of all other measurements, one-way ANOVA and Tukey post hoc tests were applied. All data were represented and evaluated with acceptable levels of significance set at $P < 0.05$ using GraphPad Prism 6 software.

Movie production

Raw movies were prepared in mp4 format, using Imaris 9.2.1 "video creation" function with 24 frame/s, 16:9 aspect ratio, 720 kbps bitrate, and H.264 codec. Movies S1 to S5 were edited and further annotated by using iMovie maker v10.1.8 (Apple, Cupertino, CA, USA).

SUPPLEMENTARY MATERIALS

Supplementary material for this article is available at http://advances.sciencemag.org/cgi/content/full/7/30/eabg5733/DC1

View/request a protocol for this paper from *Bio-protocol*.

REFERENCES AND NOTES

1. Z. M. Younossi, Non-alcoholic fatty liver disease—A global public health /perspective. *J. Hepatol.* **70**, 531–544 (2019).
2. M. M. Yeh, E. M. Brunt, Pathology of nonalcoholic fatty liver disease. *Am. J. Clin. Pathol.* **128**, 837–847 (2007).
3. A. M. Diehl, C. Day, Cause, pathogenesis, and treatment of nonalcoholic steatohepatitis. *N. Engl. J. Med.* **377**, 2063–2072 (2017).
4. S. H. Ibrahim, P. Hirsova, G. J. Gores, Non-alcoholic steatohepatitis pathogenesis: Sublethal hepatocyte injury as a driver of liver inflammation. *Gut* **67**, 963–972 (2018).
5. Y. Takahashi, T. Fukusato, Histopathology of nonalcoholic fatty liver disease/nonalcoholic steatohepatitis. *World J. Gastroenterol.* **20**, 15539–15548 (2014).
6. B. Smeuninx, E. Boslem, M. A. Febbraio, Current and future treatments in the fight against non-alcoholic fatty liver disease. *Cancers* **12**, 1714 (2020).
7. J. K. Lau, X. Zhang, J. Yu, Animal models of non-alcoholic fatty liver disease: Current perspectives and recent advances. *J. Pathol.* **241**, 36–44 (2017).
8. E. Sabath, A. Baez-Ruiz, R. M. Buijs, Non-alcoholic fatty liver disease as a consequence of autonomic imbalance and circadian desynchronization. *Obes. Rev.* **16**, 871–882 (2015).
9. C. M. Licht, S. A. Vreeburg, A. K. B. van Reedt Dortland, E. J. Giltay, W. J. G. Hoogendijk, R. H. De Rijk, N. Vogelzangs, F. G. Zitman, E. J. C. de Geus, B. W. J. H. Penninx, Increased sympathetic and decreased parasympathetic activity rather than changes in hypothalamic-pituitary-adrenal axis activity is associated with metabolic abnormalities. *J. Clin. Endocrinol. Metab.* **95**, 2458–2466 (2010).
10. E. Bruinstroop, J. Eliveld, E. Foppen, S. Busker, M. T. Ackermans, E. Fliers, A. Kalsbeek, Hepatic denervation and dyslipidemia in obese Zucker (fa/fa) rats. *Int. J. Obes. (Lond)* **39**, 1655–1658 (2015).
11. G. W. Lambert, N. E. Straznicky, E. A. Lambert, J. B. Dixon, M. P. Schlaich, Sympathetic nervous activation in obesity and the metabolic syndrome–causes, consequences and therapeutic implications. *Pharmacol. Ther.* **126**, 159–172 (2010).
12. J. H. Henriksen, S. Moller, S. Ring-Larsen, N. J. Christensen, The sympathetic nervous system in liver disease. *J. Hepatol.* **29**, 328–341 (1998).
13. M. Menacho-Márquez, R. Nogueiras, S. Fabbiano, V. Sauzeau, O. Al-Massadi, C. Diéguez, X. R. Bustelo, Chronic sympathoexcitation through loss of Vav3, a Rac1 activator, results in divergent effects on metabolic syndrome and obesity depending on diet. *Cell Metab.* **18**, 199–211 (2013).
14. C. Hurr, H. Simonyan, D. A. Morgan, K. Rahmouni, C. N. Young, Liver sympathetic denervation reverses obesity-induced hepatic steatosis. *J. Physiol.* **597**, 4565–4580 (2019).
15. A. N. Kandilis, I. P. Papadopoulou, J. Koskinas, G. Sotiropoulos, D. G. Tiniakos, Liver innervation and hepatic function: New insights. *J. Surg. Res.* **194**, 511–519 (2015).
16. I. Colle, H. Van Vlierberghe, R. Troisi, B. De Hemptinne, Transplanted liver: Consequences of denervation for liver functions. *Anat. Rec. A Discov. Mol. Cell. Evol. Biol.* **280**, 924–931 (2004).
17. K. Mizuno, Y. Ueno, Autonomic nervous system and the liver. *Hepatol. Res.* **47**, 160–165 (2017).
18. L. A. Streba, C. C. Vere, A. G. Ionescu, C. T. Streba, I. Rogoveanu, Role of intrahepatic innervation in regulating the activity of liver cells. *World J. Hepatol.* **6**, 137–143 (2014).
19. K. J. Jensen, G. Alpini, S. Glaser, Hepatic nervous system and neurobiology of the liver. *Compr. Physiol.* **3**, 655–665 (2013).
20. M. Amir, M. Yu, P. He, S. Srinivasan, Hepatic autonomic nervous system and neurotrophic factors regulate the pathogenesis and progression of non-alcoholic fatty liver disease. *Front. Med.* **7**, 62 (2020).
21. Y. Miyazawa, Y. Fukuda, M. Imoto, Y. Koyama, H. Nagura, Immunohistochemical studies on the distribution of nerve fibers in chronic liver diseases. *Am. J. Gastroenterol.* **83**, 1108–1114 (1988).
22. K. Jaskiewicz, S. C. Robson, L. Banach, Toxic hepatic injury is associated with proliferation of portal nerve fibers. *Pathol. Res. Pract.* **189**, 1191–1194 (1993).
23. Y. Matsunaga, H. Kawasaki, T. Terada, Stromal mast cells and nerve fibers in various chronic liver diseases: Relevance to hepatic fibrosis. *Am. J. Gastroenterol.* **94**, 1923–1932 (1999).
24. J. A. Lee, Q. Ahmed, J. E. Hines, A. D. Burt, Disappearance of hepatic parenchymal nerves in human liver cirrhosis. *Gut* **33**, 87–91 (1992).
25. S. W. Nam, H. J. Song, S. J. Back, T. H. Kim, S. H. Cho, J. Y. Han, K. Yoo, Y. S. Lee, K. W. Chung, Decreased hepatic nerve fiber innervation in patients with liver cirrhosis. *Gut. Liver* **1**, 165–170 (2007).
26. H. R. Ueda, A. Ertürk, K. Chung, V. Gradinaru, A. Chédotal, P. Tomancak, P. J. Keller, Tissue clearing and its applications in neuroscience. *Nat. Rev. Neurosci.* **21**, 61–79 (2020).
27. J. Chi, Z. Wu, C. H. J. Choi, L. Nguyen, S. Tegegne, S. E. Ackerman, A. Crane, F. Marchildon, M. Tessier-Lavigne, P. Cohen, Three-dimensional adipose tissue imaging reveals regional variation in beige fat biogenesis and PRDM16-dependent sympathetic neurite density. *Cell Metab.* **27**, 226–236 e223 (2018).
28. T. Liu, L. Yang, X. Han, X. Ding, J. Li, J. Yang, Local sympathetic innervations modulate the lung innate immune responses. *Sci. Adv.* **6**, eaay1497 (2020).
29. A. Alvarsson, M. Jimenez-Gonzalez, R. Li, C. Rosselot, N. Tzavaras, Z. Wu, A. F. Stewart, A. Garcia-Ocaña, S. A. Stanley, A 3D atlas of the dynamic and regional variation of pancreatic innervation in diabetes. *Sci. Adv.* **6**, eaaz9124 (2020).
30. H. Lee, J. H. Park, I. Seo, S. H. Park, S. Kim, Improved application of the electrophoretic tissue clearing technology, CLARITY, to intact solid organs including brain, pancreas, liver, kidney, lung, and intestine. *BMC Dev. Biol.* **14**, 48 (2014).
31. J. Xu, Y. Ma, T. Yu, D. Zhu, Quantitative assessment of optical clearing methods in various intact mouse organs. *J. Biophotonics* **12**, e201800134 (2019).
32. C. Adori, P. Low, R. D. Andó, L. Gutknecht, D. Pap, F. Truszka, J. Takács, G. G. Kovács, K.-P. Lesch, G. Bagdy, Ultrastructural characterization of tryptophan hydroxylase 2-specific cortical serotonergic fibers and dorsal raphe neuronal cell bodies after MDMA treatment in rat. *Psychopharmacology* **213**, 377–391 (2011).
33. Y. Watabe, K. Yoshimoto, M. Eguchi, S. Ueda, Degeneration of monoaminergic fibers in the aged micrencephalic rat. *Neurosci. Lett.* **385**, 82–86 (2005).

34. M. G. van Luijtelaar, H. W. Steinbusch, J. A. Tonnaer, Aberrant morphology of serotonergic fibers in the forebrain of the aged rat. *Neurosci. Lett.* **95**, 93–96 (1988).

35. G. J. Taborsky Jr., B. E. Dunning, P. J. Havel, B. Ahren, S. Kowalyk, M. R. Boyle, C. B. Verchere, D. G. Baskin, T. O. Mundinger, The canine sympathetic neuropeptide galanin: A neurotransmitter in pancreas, a neuromodulator in liver. *Horm. Metab. Res.* **31**, 351–354 (1999).

36. I. Valladolid-Acebes, T. Daraio, K. Brismar, T. Harkany, S. O. Ögren, T. G. M. Hökfelt, C. Bark, Replacing SNAP-25b with SNAP-25a expression results in metabolic disease. *Proc. Natl. Acad. Sci. U.S.A.* **112**, E4326–E4335 (2015).

37. L. Ala-Kokko, T. Pihlajaniemi, J. C. Myers, K. I. Kivirikko, E. R. Savolainen, Gene expression of type I, III and IV collagens in hepatic fibrosis induced by dimethylnitrosamine in the rat. *Biochem. J.* **244**, 75–79 (1987).

38. B. Lin, Y. Ma, S. Wu, Y. Liu, L. Liu, L. Wu, Novel serum biomarkers for noninvasive diagnosis and screening of nonalcoholic fatty liver disease-related hepatic fibrosis. *OMICS* **23**, 181–189 (2019).

39. N. Tanimizu, N. Ichinohe, T. Mitaka, Intrahepatic bile ducts guide establishment of the intrahepatic nerve network in developing and regenerating mouse liver. *Development* **145**, dev159095 (2018).

40. T. Miyashita, A. Takeda, M. Iwai, T. Shimazu, Single administration of hepatotoxic chemicals transiently decreases the gap-junction-protein levels of connexin 32 in rat liver. *Eur. J. Biochem.* **196**, 37–42 (1991).

41. F. G. Seseke, A. Gardemann, K. Jungermann, Signal propagation via gap junctions, a key step in the regulation of liver metabolism by the sympathetic hepatic nerves. *FEBS Lett.* **301**, 265–270 (1992).

42. V. Vasina, F. Giannone, M. Domenicali, R. Latorre, A. Berzigotti, P. Caraceni, M. Zoli, F. de Ponti, M. Bernardi, Portal hypertension and liver cirrhosis in rats: Effect of the β3-adrenoceptor agonist SR58611A. *Br. J. Pharmacol.* **167**, 1137–1147 (2012).

43. Y. S. Lin, Y. Nosaka, Y. Amakata, T. Maeda, Comparative study of the mammalian liver innervation: An immunohistochemical study of protein gene product 9.5, dopamine beta-hydroxylase and tyrosine hydroxylase. *Comp. Biochem. Physiol. A Physiol.* **110**, 289–298 (1995).

44. D. G. Tiniakos, J. A. Lee, A. D. Burt, Innervation of the liver: Morphology and function. *Liver* **16**, 151–160 (1996).

45. P. Skaaring, F. Bierring, On the intrinsic innervation of normal rat liver. Histochemical and scanning electron microscopical studies. *Cell Tissue Res.* **171**, 141–155 (1976).

46. F. D. Reilly, P. A. McCuskey, R. S. McCuskey, Intrahepatic distribution of nerves in the rat. *Anat. Rec.* **191**, 55–67 (1978).

47. A. Nobin, H. G. Baumgarten, B. Falck, S. Ingemansson, E. Moghimzadeh, E. Rosengren, Organization of the sympathetic innervation in liver tissue from monkey and man. *Cell Tissue Res.* **195**, 371–380 (1978).

48. M. K. Schäfer, L. E. Eiden, E. Weihe, Cholinergic neurons and terminal fields revealed by immunohistochemistry for the vesicular acetylcholine transporter. II. The peripheral nervous system. *Neuroscience* **84**, 361–376 (1998).

49. U. Arvidsson, M. Riedl, R. Elde, B. Meister, Vesicular acetylcholine transporter (VAChT) protein: A novel and unique marker for cholinergic neurons in the central and peripheral nervous systems. *J. Comp. Neurol.* **378**, 454–467 (1997).

50. K. Liu, L. Yang, G. Wang, J. Liu, X. Zhao, Y. Wang, J. Li, J. Yang, Metabolic stress drives sympathetic neuropathy within the liver. *Cell Metab.* **33**, 666–675.e4 (2021).

51. C. X. Yi, S. E. la Fleur, E. Fliers, A. Kalsbeek, The role of the autonomic nervous liver innervation in the control of energy metabolism. *Biochim. Biophys. Acta* **1802**, 416–431 (2010).

52. H.-R. Berthoud, Anatomy and function of sensory hepatic nerves. *Anat. Rec. A Discov. Mol. Cell. Evol. Biol.* **280**, 827–835 (2004).

53. N. Uyama, A. Geerts, H. Reynaert, Neural connections between the hypothalamus and the liver. *Anat. Rec. A Discov. Mol. Cell. Evol. Biol.* **280**, 808–820 (2004).

54. C. Adori, R. D. Andó, M. Szekeres, L. Gutknecht, G. G. Kovács, L. Hunyady, K.-P. Lesch, G. Bagdy, Recovery and aging of serotonergic fibers after single and intermittent MDMA treatment in Dark Agouti rat. *J. Comp. Neurol.* **519**, 2353–2378 (2011).

55. C. Adori, L. Glück, S. Barde, T. Yoshitake, G. G. Kovacs, J. Mulder, Z. Maglóczky, L. Havas, K. Bölcskei, N. Mitsios, M. Uhlén, J. Szolcsányi, J. Kehr, A. Rönnbäck, T. Schwartz, J. F. Rehfeld, T. Harkany, M. Palkovits, S. Schulz, T. Hökfelt, Critical role of somatostatin receptor 2 in the vulnerability of the central noradrenergic system: New aspects on Alzheimer's disease. *Acta Neuropathol.* **129**, 541–563 (2015).

56. M. G. van Luijtelaar, J. A. Tonnaer, H. W. Steinbusch, J. A. Tonnaer, H. W. Steinbusch, Aging of the serotonergic system in the rat forebrain: An immunocytochemical and neurochemical study. *Neurobiol. Aging* **13**, 201–215 (1992).

57. G. Koopmans, B. Hasse, N. Sinis, Chapter 19: The role of collagen in peripheral nerve repair. *Int. Rev. Neurobiol.* **87**, 363–379 (2009).

58. N. G. Carri, K. Rubin, D. Gullberg, T. Ebendal, Neuritogenesis on collagen substrates. Involvement of integrin-like matrix receptors in retinal fibre outgrowth on collagen. *Int. J. Dev. Neurosci.* **10**, 393–405 (1992).

59. T. Daraio, L. K. Bombek, M. Gosak, I. Valladolid-Acebes, M. S. Klemen, E. Refai, P. O. Berggren, K. Brismar, M. S. Rupnik, C. Bark, SNAP-25b-deficiency increases insulin secretion and changes spatiotemporal profile of Ca^{2+} oscillations in β cell networks. *Sci. Rep.* **7**, 7744 (2017).

60. F. D. Reilly, R. S. McCuskey, E. V. Cilento, Hepatic microvascular regulatory mechanisms. I. Adrenergic mechanisms. *Microvasc. Res.* **21**, 103–116 (1981).

61. H. Akiyoshi, T. Gonda, T. Terada, A comparative histochemical and immunohistochemical study of aminergic, cholinergic and peptidergic innervation in rat, hamster, guinea pig, dog and human livers. *Liver* **18**, 352–359 (1998).

62. T. Ueno, M. Sata, R. Sakata, T. Torimura, M. Sakamoto, H. Sugawara, K. Tanikawa, Hepatic stellate cells and intralobular innervation in human liver cirrhosis. *Hum. Pathol.* **28**, 953–959 (1997).

63. J. Y. Scoazec, L. Racine, A. Couvelard, A. Moreau, J. F. Flejou, D. Bernuau, G. Feldmann, Parenchymal innervation of normal and cirrhotic human liver: A light and electron microscopic study using monoclonal antibodies against the neural cell-adhesion molecule. *J. Histochem. Cytochem.* **41**, 899–908 (1993).

64. T. Ueno, P. Bioulac-Sage, C. Balabaud, J. Rosenbaum, Innervation of the sinusoidal wall: Regulation of the sinusoidal diameter. *Anat. Rec. A Discov. Mol. Cell. Evol. Biol.* **280**, 868–873 (2004).

65. Y. Iwakiri, Pathophysiology of portal hypertension. *Clin. Liver Dis.* **18**, 281–291 (2014).

66. M. Ryou, N. Stylopoulos, G. Baffy, Nonalcoholic fatty liver disease and portal hypertension. *Explor. Med.* **1**, 149–169 (2020).

67. D. Van der Graaff, W. J. Kwanten, F. J. Couturier, J. S. Govaerts, W. Verlinden, I. Brosius, M. D'Hondt, A. Driessen, B. Y. De Winter, J. G. De Man, P. P. Michielsen, S. M. Francque, Severe steatosis induces portal hypertension by systemic arterial hyporeactivity and hepatic vasoconstrictor hyperreactivity in rats. *Lab. Invest.* **98**, 1263–1275 (2018).

68. M. Kurosawa, T. Unno, Y. Aikawa, M. Yoneda, Neural regulation of hepatic blood flow in rats: An in vivo study. *Neurosci. Lett.* **321**, 145–148 (2002).

69. K. M. Hanson, Escape of the liver vasculature from adrenergic vasoconstriction. *Proc. Soc. Exp. Biol. Med.* **141**, 385–390 (1972).

70. C. V. Greenway, A. E. Lawson, S. Mellander, The effects of stimulation of the hepatic nerves, infusions of noradrenaline and occlusion of the carotid arteries on liver blood flow in the anaesthetized cat. *J. Physiol.* **192**, 21–41 (1967).

71. R. T. Mathie, V. Ralevic, G. Burnstock, Portal vascular responsiveness to sympathetic stimulation and nitric oxide in cirrhotic rats. *J. Hepatol.* **25**, 90–97 (1996).

72. J. U. Johansson, J. Ericsson, J. Janson, S. Beraki, D. Stanić, S. A. Mandic, M. A. Wikström, T. Hökfelt, S. O. Ögren, B. Rozell, P. O. Berggren, C. Bark, An ancient duplication of exon 5 in the Snap25 gene is required for complex neuronal development/function. *PLOS Genet.* **4**, e1000278 (2008).

73. Y. N. Tallini, B. Shui, K. S. Greene, K. Y. Deng, R. Doran, P. J. Fisher, W. Zipfel, M. I. Kotlikoff, BAC transgenic mice express enhanced green fluorescent protein in central and peripheral cholinergic neurons. *Physiol. Genomics* **27**, 391–397 (2006).

74. V. Sauzeau, M. A. Sevilla, J. V. Rivas-Elena, E. de Álava, M. J. Montero, J. M. López-Novoa, X. R. Bustelo, Vav3 proto-oncogene deficiency leads to sympathetic hyperactivity and cardiovascular dysfunction. *Nat. Med.* **12**, 841–845 (2006).

75. K. H. Chang, A. Sanchez-Aguilera, S. Shen, A. Sengupta, N. M. Madhu, A. M. Ficker, S. K. Dunn, A. M. Kuenzi, J. L. Arnett, R. A. Santho, X. Agirre, J. P. Perentesis, M. W. Deininger, Y. Zheng, X. R. Bustelo, D. A. Williams, J. A. Cancelas, Vav3 collaborates with p190-BCR-ABL in lymphoid progenitor leukemogenesis, proliferation, and survival. *Blood* **120**, 800–811 (2012).

76. L. Horvathova, A. Padova, A. Tillinger, J. Osacka, J. Bizik, B. Mravec, Sympathectomy reduces tumor weight and affects expression of tumor-related genes in melanoma tissue in the mouse. *Stress* **19**, 528–534 (2016).

77. P. Bedossa, C. Poitou, N. Veyrie, J. L. Bouillot, A. Basdevant, V. Paradis, J. Tordjman, K. Clement, Histopathological algorithm and scoring system for evaluation of liver lesions in morbidly obese patients. *Hepatology* **56**, 1751–1759 (2012).

78. N. Renier, E. L. Adams, C. Kirst, Z. Wu, R. Azevedo, J. Kohl, A. E. Autry, L. Kadiri, K. Umadevi Venkataraju, Y. Zhou, V. X. Wang, C. Y. Tang, O. Olsen, C. Dulac, P. Osten, M. Tessier-Lavigne, Mapping of brain activity by automated volume analysis of immediate early genes. *Cell* **165**, 1789–1802 (2016).

79. J. Kehr, T. Yoshitake, Monitoring brain chemical signals by microdialysis, in *Encyclopedia of Sensors*, C. A. Grimes, E. C. Dickey, M. V. Pishko, Eds. (American Scientific Publishers, 2006), vol. 6, pp. 287–312.

80. J. O. Strom, T. Nilsson, E. Theodorsson, Effects of 17β-estradiol on galanin(1-29)- and galanin(1-16)-like immunoreactivities. *Peptides* **43**, 1–7 (2013).

81. E. Theodorsson-Norheim, A. Hemsen, J. M. Lundberg, Radioimmunoassay for neuropeptide Y (NPY): Chromatographic characterization of immunoreactivity in plasma and tissue extracts. *Scand. J. Clin. Lab. Invest.* **45**, 355–365 (1985).

82. E. Theodorsson, O. Rugarn, Radioimmunoassay for rat galanin: Immunochemical and chromatographic characterization of immunoreactivity in tissue extracts. *Scand. J. Clin. Lab. Invest.* **60**, 411–418 (2000).

83. D. Stanic, E. Kuteeva, I. Nylander, T. Hokfelt, Characterization of CGRP protein expression in "satellite-like" cells and dendritic arbours of the mouse olfactory bulb. *J. Comp. Neurol.* **518**, 770–784 (2010).

84. D. Marsh, J. Grassi, M. Vigny, J. Massoulie, An immunological study of rat acetylcholinesterase: Comparison with acetylcholinesterases from other vertebrates. *J. Neurochem.* **43**, 204–213 (1984).

85. I. Tooyama, H. Kimura, A protein encoded by an alternative splice variant of choline acetyltransferase mRNA is localized preferentially in peripheral nerve cells and fibers. *J. Chem. Neuroanat.* **17**, 217–226 (2000).

86. S. Kobayashi, Y. Tomiyama, Y. Hoyano, Y. Yamazaki, H. Kusama, Y. Itoh, Y. Kubota, K. Kohri, Gene expressions and mechanical functions of α1-adrenoceptor subtypes in mouse ureter. *World J. Urol.* **27**, 775–780 (2009).

87. B. W. Renz, R. Takahashi, T. Tanaka, M. Macchini, Y. Hayakawa, Z. Dantes, H. C. Maurer, X. Chen, Z. Jiang, C. B. Westphalen, M. Ilmer, G. Valenti, S. K. Mohanta, A. J. R. Habenicht, M. Middelhoff, T. Chu, K. Nagar, Y. Tailor, R. Casadei, M. D. Marco, A. Kleespies, R. A. Friedman, H. Remotti, M. Reichert, D. L. Worthley, J. Neumann, J. Werner, A. C. Iuga, K. P. Olive, T. C. Wang, β2 adrenergic-neurotrophin feedforward loop promotes pancreatic cancer. *Cancer Cell* **33**, 75–90.e7 (2018).

88. P. Procacci, V. Magnaghi, E. Pannese, Perineuronal satellite cells in mouse spinal ganglia express the gap junction protein connexin43 throughout life with decline in old age. *Brain Res. Bull.* **75**, 562–569 (2008).

Science Advances

Disorganization and degeneration of liver sympathetic innervations in nonalcoholic fatty liver disease revealed by 3D imaging

Csaba AdoriTeresa DaraioRaoul KuiperSwapnali BardeLubica HorvathovaTakashi YoshitakeRobert IhnatkoIsmael Valladolid-AcebesPauline VercruysseAshley M. WellendorfRoberto GramignoliBela BozokyJan KehrElvar TheodorssonJose A. CancelasBoris MravecCarl JornsEwa EllisJan MulderMathias UhlénChristina BarkTomas Hökfelt

View the article online
https://www.science.org/doi/10.1126/sciadv.abg5733
Permissions
https://www.science.org/help/reprints-and-permissions

Use of think article is subject to the Terms of service